

Fundamental Properties and Distances of LMC Eclipsing Binaries: IV. HV 5936¹

E.L. Fitzpatrick^{1,4}, I. Ribas^{2,4}, E.F. Guinan¹, F.P. Maloney¹, A. Claret³

ABSTRACT

We have determined the fundamental properties and distance of a fourth eclipsing binary system (EB) in the Large Magellanic Cloud, HV 5936 (\sim B0.5 V + \sim B2 III). As in our previous studies, we combine “classical” EB light curve and radial velocity curve analyses with modeling of the UV-through-optical spectral energy distribution of HV 5936 to produce a detailed characterization of the system. In this paper, we also include an analysis of the high-resolution optical absorption line spectra of the binary components. We find HV 5936 to be an Algol-class system, in which the masses of the primary and secondary stars have evolved via mass transfer to their current values of $11.6 M_{\odot}$ and $4.7 M_{\odot}$, respectively. The properties of the primary star are indistinguishable from those of a “normal” star of the same current mass. The secondary is found to be overluminous for its current mass and exhibits a factor-of-2 enhancement in its surface He abundance. These results are compatible with “Case A” mass exchange occurring during the core hydrogen burning phase of the current secondary. The distance derived to the system, 43.2 ± 1.8 kpc, implies a distance of ~ 44.3 to the optical center of the LMC. This is several kpc closer than found in our analyses of other systems and we suggest that HV 5936 lies “above” the LMC disk. This is supported by the very low interstellar H I column density and low $E(B - V)$ found for the system — both of which are consistent with expected Milky Way foreground material — and may be associated with HV 5936’s location near the LMC supergiant shell LMC 4.

¹Department of Astronomy & Astrophysics, Villanova University, Villanova, PA 19085, USA

²Departament d’Astronomia i Meteorologia, Universitat de Barcelona, Av. Diagonal, 647, E-08028 Barcelona, Spain

³Instituto de Astrofísica de Andalucía, CSIC, Apartado 3004, E-18080 Granada, Spain

⁴Visiting Astronomer, Cerro Tololo Inter-American Observatory, National Optical Astronomy Observatories, which is operated by the Association of Universities for Research in Astronomy, Inc. (AURA) under cooperative agreement with the National Science Foundation.

Subject headings: Binaries: Eclipsing - Stars: Distances - Stars: Fundamental Parameters - Stars: Individual (HV 5936) - Galaxies: Magellanic Clouds - Cosmology: Distance Scale

1. Introduction

This is the fourth in a series of papers presenting results from detailed analyses of B-type eclipsing binary (EB) systems in the Large Magellanic Cloud (LMC). Our primary scientific goals are: 1) to determine an essentially complete description of the stellar properties of each system, thus providing tests and constraints for stellar evolution theory; and 2) to measure precise individual distance for each system, from which the general distance to the LMC can be derived. Because of its role as a fundamental calibrator for distance indicators, the LMC’s distance is particularly important for determining the size scale of the Universe, and its current uncertainty of 10-15% contributes considerably to the uncertainty in the Hubble Constant (e.g., Mould et al. 2000).

In our previous studies, we examined the LMC EB systems HV 2274 (Guinan et al. 1998, hereafter “Paper I”; Ribas et al. 2000a), HV 982 (Fitzpatrick et al. 2002, “Paper II”), and EROS 1044 (Ribas et al. 2002, “Paper III”). The apparent locations of these systems in the LMC can be seen in Figure 1. The results of these analyses are beautifully consistent with expectations from stellar structure theory and provide strong constraints on the distance to the LMC. As discussed in Paper III, the three individual distances are all consistent with a mean of ~ 48 kpc, although there is a suggestion that HV 982 and, by association, perhaps the general 30 Doradus region, may lie behind the LMC’s “Bar”, by several kpc. Conclusions about the LMC’s distance are somewhat dependent on assumptions about its spatial orientation and need to be strengthened with additional measurements from the remaining eclipsing binaries in our program. Our approach is ideally suited to pursuing the issues of the spatial orientation, structure, and general distance to the LMC, since we measure precise distances to individuals systems which are widely spread across the face of the LMC.

In this paper, we apply our analysis to a fourth LMC B-type EB, HV 5936, and derive its stellar properties and distance. This system, with $V \simeq 14.8$, stands in some contrast

¹Based on observations with the NASA/ESA Hubble Space Telescope, obtained at the Space Telescope Science Institute, which is operated by the Association of Universities for Research in Astronomy, Inc. under NASA contract No. NAS5-26555.

to those in our previous studies in both its composition and its location. HV 5936 is a semidetached system, in which the cooler, less massive component fills completely its Roche lobe. Thus, the currently more massive (and more luminous) component began its life as the junior, lower mass member of the binary. This provides an excellent opportunity to examine the characteristics of the massive component, which — due to the rapid dynamical relaxation expected to follow mass transfer — should be indistinguishable from a “normal” star of the same current mass. In addition to this feature, HV 5936 is located in a very different part of the LMC from our previous targets (see Fig. 1), lying several degrees north of the LMC’s Bar and superimposed on a well known “hole” in the LMC’s H I distribution (McGee & Milton 1966), corresponding to the supergiant shell LMC 4 (Meaburn 1980). Its distance should reflect strongly the spatial orientation of the LMC, i.e., its inclination angle and line of nodes orientation, and could provide constraints on these factors.

The structure of this paper is similar to our earlier works. In §2 we describe the data included in the study. In §3 we describe, and present the results from, our standard analysis, which incorporates the binary’s light curve, radial velocity curve, and UV-through-optical spectral energy distribution. A study of the high-resolution optical spectrum of the HV 5936 components is presented in §4. We combine all our results and give a detailed characterization of the properties and likely history of the HV 5936 system in §5. Some aspects of our results relating to the interstellar medium towards HV 5936 are described in §6, including an indication of the relative location of HV 5936 within the LMC. Finally, we derive the distance to the system and compare it with our previous results in §7 and provide some summary comments in §8.

2. The Data

Three distinct datasets are required to carry out our analyses of the LMC EB systems: precise differential photometry (yielding light curves), medium-resolution spectroscopy (yielding radial velocity curves), and multiwavelength spectrophotometry (yielding temperature and reddening information). Each of these three datasets are described briefly below. As in our previous papers, the primary (P) and secondary (S) components of the HV 5936 system are defined photometrically and refer to the hotter and cooler components, respectively.

2.1. Optical Photometry

CCD differential photometric observations of HV 5936 were reported by Jensen, Clausen, & Giménez (1988). These data were obtained between 1983 and 1984 with a 1.54-m telescope at the European Southern Observatory (La Silla, Chile). The published light curves, obtained in the Johnson B and V passbands, have fairly good phase coverage, with 44 and 144 measurements, respectively. According to Jensen et al., the precision of the individual differential photometric measurements is better than 0.010 mag. In this study, we adopt the orbital ephemeris determined by Jensen et al.:

$$T(\text{Min I}) = \text{HJD}2445657.7911 + 2.8050681 E$$

2.2. Optical Spectroscopy

Radial velocity curves for HV 5936, and a number of other LMC EBs, were derived from optical echelle spectra obtained by us during 6-night and 8-night observing runs in January and December 2000, respectively, with the Blanco 4-m telescope at Cerro Tololo Inter-American Observatory in Chile. The seeing conditions during the two runs ranged between 0.7 and 1.8 arcsec. We secured eighteen spectra of HV 5936 – near orbital quadratures – covering the wavelength range 3600–5500 Å, with a spectral resolution of $\lambda/\Delta\lambda \simeq 22,000$, and a S/N of $\sim 20:1$. The plate scale of the data is $0.08 \text{ \AA pix}^{-1}$ ($5.3 \text{ km s}^{-1} \text{ pix}^{-1}$) and there are 2.6 pixels per resolution element. Identical instrumental setups were used for both observing runs. The exposure time per spectrum was 1800 sec, sufficiently short to avoid significant radial velocity shifts during the integrations. All the HV 5936 observations were bracketed with ThAr comparison spectra for proper wavelength calibration. The raw images were reduced using standard NOAO/IRAF tasks (including bias subtraction, flat field correction, sky-background subtraction, cosmic ray removal, extraction of the orders, dispersion correction, merging, and continuum normalization).

A typical spectrum is shown in Figure 2. The H I Balmer lines and the strongest He I features are labeled, with arrows marking the expected line positions for the two components of the system (according to the radial velocity curve solution described in §3.2). This spectrum was obtained at orbital phase 0.30 and illustrates the clean velocity separation of the two components of the binary.

To determine the radial velocities of HV 5936’s two components from the echelle spectra, we followed the procedure described in Paper II utilizing the KOREL program (Hadrava 1995, 1997). KOREL is based on the “spectral disentangling” technique, which assumes that an observed double-lined spectrum is a simple linear combination of two single-lined spectra

whose velocities reflect the orbital properties of the system. When applied to a set of spectra — obtained over a range of orbital phases — KOREL yields component velocities (relative to the system barycenter) for each individual spectrum and “disentangled” spectra for each of the two binary members, combining information from the whole ensemble of spectra. We applied the KOREL analysis to our echelle data in the 4000–5000 Å wavelength region. The H β , H γ and H δ lines were excluded by setting the normalized flux to unity in a window around their central wavelength. To translate the velocities to the heliocentric system, we determined the systemic velocity of HV 5936 from the individual disentangled spectra. Cross-correlation of these extracted spectra with a high S/N (~ 250) observed spectrum (HR 1443, B2 IV-V) and with a synthetic template yielded values consistent with a systemic velocity of $v_\gamma = +314.3 \pm 5.8 \text{ km s}^{-1}$.

Table 2 lists the heliocentric radial velocities derived from all the CTIO spectra using the procedure outlined above (“RV $_P$ ” and “RV $_S$ ”). Also listed are the dates of observation and the corresponding phases. A large number of KOREL runs from different starting points were carried out to explore the parameter space and make realistic estimations of the uncertainties. A detailed discussion of these is left for §3.2.

The individual disentangled spectra of the primary and secondary provide valuable insight into the nature of the HV 5936 system, as well as confirmation of the results from our general analysis. These spectra are discussed in §4.

2.3. UV/Optical Spectrophotometry

We obtained spectrophotometric observations of HV 5936 at UV and optical wavelengths with the *Hubble Space Telescope* using both the Faint Object Spectrograph (FOS) and the Space Telescope Imaging Spectrograph (STIS). These data are summarized in Table 1.

The FOS observations utilized the $3.7'' \times 1.3''$ aperture, yielding a spectral resolution of $\lambda/\Delta\lambda \simeq 1300$. The four individual spectra were processed and calibrated using the standard pipeline processing software for the FOS and then merged to form a single spectrum which covers the range 1145 Å to 4790 Å. The STIS observations utilized the $52'' \times 0.5''$ aperture, yielding a spectral resolution of $\lambda/\Delta\lambda \simeq 750$. These data were processed and calibrated using the standard pipeline processing software. Cosmic ray blemishes were cleaned “by hand” and the G430L and G750L spectra were trimmed to the regions 3510–5690 Å and 5410–7490 Å, respectively. Because of concerns about the photometric zeropoints and stability, the two STIS spectra were not merged (see §3.3).

3. The Analysis

Our study of HV 5936 proceeds from three separate but interdependent analyses. These involve the radial velocity curve, the light curve, and the spectral energy distribution (SED). The combined results provide essentially a complete description of the gross physical properties of the HV 5936 system and a precise measurement of its distance. Each of the three analyses is described below.

3.1. The Light Curve

The fits to the light curves were carried out using an improved version of the Wilson-Devinney (W-D) program (Wilson & Devinney 1971) that includes a model atmosphere routine developed by Milone, Stagg & Kurucz (1992) for the computation of the stellar radiative parameters. Both detailed reflection model (MREF=2, NREF=1) and proximity effect corrections were taken into account when fitting the light curves. The bolometric albedo and the gravity-brightening coefficients were both set at the canonical value of 1.0 for stars with radiative envelopes. For the limb darkening we used a logarithmic law as defined in KlingleSmith & Sobieski (1970), with first- and second-order coefficients interpolated at each iteration for the exact T_{eff} and $\log g$ of each component from a set of tables computed in advance using a grid of ATLAS9 model atmospheres. A mass ratio of $q = M_S/M_P = 0.407$ was adopted from the spectroscopic solution (§3.2), and the temperature of the primary component was set to $T_{\text{eff}}^P = 26,450$ K, as discussed in §3.3. We have adopted a circular orbit as suggested by the equal width of the eclipses and the occurrence of the secondary eclipse at exactly phase 0.5. Further support for this comes from the fact that the system is semidetached (see below) and orbital circularization takes place over a very short timescale. Finally, the rotational velocity of the primary star was set to 1.25 times the synchronous rate and the secondary star was adopted to rotate synchronously. A discussion of the component’s rotational velocities is provided in §4.

Our initial light curve fits were run with a detached configuration (W-D mode 2). However, preliminary tests indicated a rapid decrease of the surface gravitational potential of the secondary component until reaching its critical value. Several runs from different starting values confirmed this behavior. Therefore, all further W-D solutions were run in mode 5, i.e., secondary component filling its Roche critical surface. According to this, HV 5936 is a semidetached binary where the cooler, less massive component appears to be more evolved and fills its Roche lobe. This is the classical configuration of post-mass transfer Algol-class systems.

In our final analysis we solved for the following light curve parameters: the orbital inclination (i), the temperature of the secondary ($T_{\text{eff}}^{\text{S}}$), the gravitational potential of the primary⁶ (Ω_{P}), the luminosity of the primary (L_{P}), and a phase offset ($\Delta\phi$) which accounts for possible inaccuracy in the adopted ephemeris reference epoch. The iterations with the W-D code were carried out automatically until convergence, and a solution was defined as the set of parameters for which the differential corrections suggested by the program were smaller than the internal probable errors on three consecutive iterations. As a general rule, several runs with different starting parameters are used to make realistic estimates of the uncertainties and to test the uniqueness of the solution.

Because of the relatively small number of free parameters and the constraint provided by the semidetached configuration, convergence was achieved rapidly in the light curve fits. The r.m.s. residuals were determined to be 0.010, and 0.009 mag for the B and V light curves, respectively. These values are approximately equal to the observed scatter of the observations. The resulting orbital and physical parameters are well-defined and the best-fitting model light curves, together with the O–C residuals, are shown in Figure 4. As can be seen in the figure, a small systematic departure of the fit arises in the first quadrature (phase 0.2–0.4) of the V light curve. This cannot be confirmed in the B light curve because of the lack of photometric coverage. It is uncertain at this point whether this is a real effect or just an artifact of the photometric reduction. If it were real, the asymmetry of the quadrature maxima could arise from the presence of a hot spot on the primary component. This is not unexpected in an Algol system because active mass transfer could be taking place and a hot spot in the atmosphere of the hotter component might arise from the impact of the accreting material and subsequent kinetic heating. We explored this scenario by running W-D solutions with an area on the primary component 10% hotter than the rest of the atmosphere. The systematic trend in the residuals did indeed disappear when the spot was included but this is not surprising because we added two new free parameters in the analysis (spot radius and location). The new r.m.s. residuals were found to be 0.009 and 0.008 mag for the B and V light curves, respectively. The solution with the hot spot is very similar but yields a radius for the primary component about 2% smaller and a temperature ratio about 5% larger. In the absence of conclusive evidence, we decided to adopt the “unperturbed” solution without a hot spot. Besides, the resulting spot location is not consistent with the expected impact site of a putative stream of matter using the model of Lubow & Shu (1975). (Note that the fractional radius of the primary component is sufficiently large to prevent the formation of a stable accretion disk (e.g. Albright & Richards 1993).)

⁶Note that the surface gravitational potential of the secondary is constrained by the semidetached condition.

As is evident from Figure 4, the light curves of HV 5936 display rather prominent out-of-eclipse variability. This arises chiefly from variations in the effective radiating area of the secondary star. Due to its non-spherical shape (filling its Roche lobe), the surface area of the secondary star changes with the orbital phase and so does its total brightness. The stellar cross-section reaches a maximum at the orbital quadratures and a minimum at the eclipses. Another factor contributing to the out-of-eclipse variation is irradiation. This is a rather significant effect in Algols because the secondary star is often larger but cooler than the primary. Thus, when the primary component is in front (near the phase of the secondary eclipse), we see its light reflected off the atmosphere of the secondary star. This causes the ingress and egress of the secondary eclipse to be brighter than the ingress and egress of the primary eclipse. Both effects discussed here are fully accounted for by the physical model upon which W-D is based, as proven by the excellent fit to the light curves.

The final orbital and stellar parameters adopted from the light curve analysis are listed in Table 3. The uncertainties given in this table were not adopted from the formal probable errors provided by the W-D code, but instead from numerical simulations and other considerations. Several sets of starting parameters were tried in order to explore the full extent of the parameter space. In addition, the W-D iterations were not stopped after a solution was found, instead, the program was kept running to test the stability of the solution and the geometry of the χ^2 function near the minimum. The scatter in the resulting parameters from numerous additional solutions yielded estimated uncertainties that we consider to be more realistic, and are generally several times larger than the internal statistical errors.

As an internal consistency check, we re-analyzed the light curves with the mass ratio q left as a free parameter, rather than fixing it to the spectroscopically determined value. This test yielded a “photometric mass ratio” of $q_{\text{ptm}} = 0.417 \pm 0.031$ which is in excellent agreement with the spectroscopic result of $q = 0.407 \pm 0.016$ (see §3.2). Photometric estimates of q are strongly dependent on outside-of-eclipse light variations which, in the case of HV 5936, arise primarily from the changing aspects of the tidally distorted stars (as well as the reflection effect). The good agreement of q_{ptm} with the directly determined spectroscopic mass ratio indicates that the light curves are essentially free of significant perturbing effects from gas flows and accretion heating — consistent with our conclusion above from examining the residuals to the light curve fits. This agreement reaffirms that the orbital and stellar properties determined from the combined solutions of light and radial velocity curves are both self-consistent and robust.

The same light curves as analyzed here (i.e., from Jensen et al. 1988) have also been studied by Bell et al. (1993). Those authors employed two different light-curve synthesis programs, one of which was a 1983 version of the W-D code. Their solutions were run with

a mass ratio quite different from ours ($q_{\text{Bell}} = 0.46$) and this resulted in a larger fractional radius for the secondary component than we find. Also, their adopted temperature for the primary was about 3000 K larger than our value. Apart from those, the rest of the light curve parameters obtained by Bell et al. are compatible with the ones listed in Table 3. It should be mentioned, however, that our fits display significantly smaller residuals, which probably result from a better-determined mass ratio and the more sophisticated fitting program that we have employed.

3.2. The Radial Velocity Curve

The radial velocity curve was fit using the same version of the W-D program as described above. The free parameters were: the orbital semi-major axis (a), the mass ratio (q), and a velocity zero point (the systemic radial velocity v_γ). The rest of the parameters were set to those resulting from the light curve solutions discussed in the previous section. The best fit to the radial velocity curve is shown in Figure 3. The fit residuals correspond to r.m.s. internal errors of 1.2 and 2.8 km s⁻¹ for the primary and secondary components, respectively. The relatively large difference between these residuals is a consequence of the secondary star being significantly less luminous, and thus its velocities have intrinsically larger errors.

The parameters resulting from the radial velocity curve fit are listed in Table 3. The uncertainties given in the table are not taken directly from the W-D output, since they fail to account for any systematic effects that could be present in the velocity data. Instead, we estimated more realistic errors by considering the scatter of the velocities derived from the disentangling analysis of separate spectral regions. Thus, we divided our entire spectrum into four wavelength intervals and analyzed these separately with KOREL. The standard deviation of the resulting velocities was found to be 3.2 and 7.5 km s⁻¹ for the primary and secondary components, respectively. We conservatively adopted these values as the uncertainty of the velocity semi-amplitudes and scaled the rest of the parameter errors listed in Table 3 accordingly.

Independent radial velocity observations were secured and analyzed by Bell et al. (1993). According to these authors, the observations were acquired in less-than-perfect conditions, with atmospheric seeing of 3–6 arcsec and intermittent clouds. Their resulting radial velocity curves have large scatter, with “O–C” residuals up to 80 km s⁻¹. The better quality of our radial velocity data is due to both the excellent atmospheric conditions at CTIO and the use of the spectral disentangling technique, which has been proved to be superior to classical cross-correlation. When comparing the solutions, the value of the velocity that Bell et al. report for the primary (more luminous) component is in excellent agreement with our

determination listed in Table 3. However, the velocity semiamplitude of the less luminous component, more severely affected by poor-quality observations, found by Bell et al. is much smaller ($\sim 50 \text{ km s}^{-1}$; 3.5σ) than our value.

3.3. The UV/Optical Energy Distribution

3.3.1. The Basics

In general, the observed SED $f_{\lambda\oplus}$ of a binary system can be expressed as:

$$f_{\lambda\oplus} = \left(\frac{R_P}{d}\right)^2 [F_\lambda^P + (R_S/R_P)^2 F_\lambda^S] \times 10^{-0.4E(B-V)[k(\lambda-V)+R(V)]} \quad (1)$$

where F_λ^i $\{i = P, S\}$ are the surface fluxes of the primary and secondary stars, the R_i are the absolute radii of the components, and d is the distance to the binary. The last term carries the extinction information, including $E(B - V)$, the normalized extinction curve $k(\lambda - V) \equiv E(\lambda - V)/E(B - V)$, and the ratio of selective-to-total extinction in the V band $R(V) \equiv A(V)/E(B - V)$. In our studies, we represent the stellar surface fluxes with R.L. Kurucz’s ATLAS9 atmospheres and use a parameterized representation of UV-through-IR extinction based on the work of Fitzpatrick & Massa (1990) and Fitzpatrick (1999; hereafter F99). The Kurucz models are each functions of four parameters (T_{eff} , $\log g$, $[\text{m}/\text{H}]$, and microturbulence velocity v_{micro}), and the extinction curves are functions of six parameters (see F99). Note that, for the purposes of Eq. 1, it does not matter which star in a system is identified as the primary.

We model the observed SED by performing a non-linear least squares fit to determine the best-fit values of all parameters which contribute to the right side of equation 1. For HV 5936 (and as for our previous studies), we can make several simplifications which reduce the number of free parameters in the problem: (1) the temperature ratio of the two stars is known from the light curve analysis; (2) the surface gravities can be determined by combining results from the light and radial velocity curve analyses and are $\log g = 3.98$ and 3.49 for the primary and secondary stars, respectively (see §5); (3) the values of $[\text{m}/\text{H}]$ and v_{micro} can be assumed to be identical for both components; (4) the ratio R_S/R_P is known; and (5) the standard mean value of $R(V) = 3.1$ found for the Milky Way can reasonably be assumed given the existing LMC measurements (e.g., Koornneef 1982; Morgan & Nandy 1982; see §6).

We prepared the spectrophotometric datasets for the SED analysis by (1) velocity-shifting to bring the centroids of the stellar features to rest velocity; (2) correcting for

the presence of a strong interstellar H I Ly α absorption feature in the FOS spectrum at 1215.7 Å (see §6); and (3) binning to match the ATLAS9 wavelength grid. The statistical errors assigned to each bin were computed from the statistical errors of the original data, i.e., $\sigma_{\text{bin}}^2 = 1/\Sigma(1/\sigma_i^2)$, where the σ_i are the statistical errors of the individual spectrophotometric data points within a bin. For all the spectra, these binned uncertainties typically lie in the range 0.5% to 1.5% of the binned fluxes. The weighting factor for each bin in the least squares procedure is given by $w_{\text{bin}} = 1/\sigma_{\text{bin}}^2$. We exclude a number of individual bins from the fit (i.e., set the weight to zero) for the reasons discussed by FM99 (mainly due to the presence of interstellar gas absorption features).

As discussed in Paper II, we do not merge the FOS and STIS data into a single spectrum, but rather perform the fit on the three binned spectra simultaneously and independently. We assume that the FOS fluxes represent the “true” flux level and account for zero point uncertainties in the STIS data by incorporating two zeropoint corrections (one for each STIS spectrum) in the fitting procedure. We later explicitly determine the uncertainties in the results introduced by zeropoint uncertainties in FOS.

3.3.2. Special Considerations for HV 5936

As noted in §2.1, the out-of-eclipse variations seen in HV 5936’s light curve result primarily from changes in the apparent size (i.e., as presented toward the Earth) of the secondary due to its mild non-sphericity and also from phase-modulated reflection of light from the primary off the secondary. These effects must be taken into account in the SED analysis because they affect the relative contributions of primary and secondary light to the observed SED.

We incorporate the effects through a simple modification of Eq. 1:

$$f_{\lambda\oplus} = \left(\frac{R_P}{d}\right)^2 [k_P F_\lambda^P + k_S (R_S/R_P)^2 F_\lambda^S] \times 10^{-0.4E(B-V)[k(\lambda-V)+R(V)]} \quad (2)$$

where k_P and k_S are phase-dependent correction factors accounting for additional reflected light from the primary and the varying apparent size of the secondary, respectively. The values of k_P and k_S for each of the spectrophotometric observations are listed in Table 1 and were computed from the results of the W-D light curve analysis. The k_P are always greater than 1, since reflection always adds otherwise-unseen light from the primary. The value of k_S for the FOS/G130H spectrum indicates that, at the phase of this observation, the apparent size of the secondary was slightly smaller than its mean value (as given by the “volume radius” computed by the W-D program). For all the other spectra, the apparent

size of the secondary was larger than its mean value. Note that all the corrections for the FOS datasets — which provide the photometric zeropoint for the SED analysis — are very close to 1.0.

3.3.3. Results

We computed the final fit to HV 5936’s SED utilizing Eq. 2 with the appropriate values of k_P and k_S inserted for each dataset. As in previous papers, we adjusted the weights in the fitting procedure to yield a final value of $\chi^2 = 1$ — since the statistical errors of the data under-represent the total uncertainties (see the discussion in Paper II). This was accomplished by quadratically adding an uncertainty equivalent to 1.9% of the local binned flux to the statistical uncertainty of each flux point. (Essentially identical results occur if the statistical errors are simply scaled by a factor of 2.2 to yield $\chi^2 = 1$.) This value of 1.9% gives an indication of the general quality of the fit to HV 5936’s SED, excluding the effect of statistical noise. It is comparable the quality level we have seen in the previous analyses.

The best-fitting values of the energy distribution parameters for HV 5936 and their associated 1σ uncertainties (“internal errors”) are listed in Tables 3 (stellar properties), 4 (STIS offsets), and 5 (extinction curve parameters). A comparison between the observed spectra and the best-fitting model is shown in Figure 5. The three binned spectra are plotted separately in the figure for clarity (small filled circles). The zeropoint offset corrections (see Table 4) were applied to all STIS spectra in Figure 5. Note that we show the quantity $\lambda f_{\lambda\oplus}$ as the ordinate in Figure 5 (rather than $f_{\lambda\oplus}$) strictly for plotting purposes, to “flatten out” the energy distributions.

The correction factors of 10.2% and 5.9% are required to rectify the STIS G430L and G750L spectra, respectively, are similar to the results found in Papers II and III. This apparently systematic effect probably results from small light losses in the STIS 0’5 slit. This will be tested by using a wider slit in future STIS observations.

4. Supplemental Analysis of the “Disentangled” Spectra

In §2.2, we utilized the KOREL program primarily to determine the radial velocities of HV 5936’s component stars. However, byproducts of this program, i.e., a high-resolution, “disentangled” optical spectrum for each star, can provide valuable additional information on the binary system which is *entirely independent* of the analysis described in the preceding section. This information can be tapped by modeling these absorption line spectra with

synthetic spectra. The potential value of such an analysis is threefold, since it can: 1) add new information on the system, 2) independently verify results of the preceding analysis, or 3) identify problems with the preceding analysis.

The disentangled spectra of HV 5936’s two components, as produced by the KOREL program are shown in Figures 6 and 7. Each spectrum has a resolution of $\sim 0.2 \text{ \AA}$ and consists of 12,453 data points. The most prominent features in both are lines of H I and He I. The strong C II $\lambda 4267$ and Si III $\lambda\lambda 4553, 4568, 4574$ lines are noted in the primary’s spectrum (Fig. 6). Virtually all the other, weaker absorption features in that spectrum are due to lines of O II. There are no positive identifications of individual metal absorption lines in the noisier spectrum of the secondary. The ripple-like structure in the range 4140–4170 \AA of both spectra (near the position of a He I line) is an artifact of the KOREL program, and results because the observations were mainly obtained near orbital quadratures and not distributed more uniformly throughout the orbit. The strengths of all the lines in these two spectra are diluted by the presence of continuum light from both binary components. Given the phase distribution of the original optical data (see Table 2), we compute that the primary and secondary contribute 63.9% and 36.1%, respectively, of the continuum light in these mean spectra. These values incorporate the reflection and ellipticity effects noted in §3, and have uncertainties of order $\sim 1\%$. In Figures 6 and 7, we have adjusted the vertical axes so that the lines are in their correct strengths relative to the bottoms of each panel.

We model the disentangled spectra by utilizing ATLAS9 atmospheric structure models, Ivan Hubeny’s spectral synthesis program SYNSPEC, and essentially the same χ^2 -minimization technique as described in §3.3 for the SED analysis. In general, finding the best-fitting synthetic spectrum for these stars requires the determination of seven parameters. Four of these — T_{eff} , $\log g$, $[\text{m}/\text{H}]$, and v_{micro} — are required to specify the appropriate ATLAS9 model. Two more — v_{radial} and $v \sin i$ (along with v_{micro}) — are used explicitly by SYNSPEC in determining line positions and widths. A final parameter, which we characterize as the percent contribution of each star to the observed continuum, is required to reproduce the dilution of the line strengths. For the case of the HV 5936 stars, we found that the microturbulence velocity was poorly determined and so we simply adopted the value of 2.6 km s^{-1} derived in the SED analysis in §3.3. In addition, we simultaneously determined the coefficients of a high-order Legendre polynomial to allow the smoothing out of “bumps and wiggles” which can be seen in the spectra of both stars. These result from deficiencies in the normalization of the original echelle spectra used by KOREL. The 4140–4170 \AA region, noted above, was excluded from all fits.

When analyzing the primary’s spectrum we found that the results of the fitting procedure depended somewhat on the assumed order of the normalizing function. Therefore, we

performed 7 independent fits, utilizing 10, 15, 20, 25, 30, 35, or 40 order Legendre polynomials. These sample the reasonable range, since a polynomial with fewer than 10 orders cannot match the observed structure in the continuum, while those with more than 40 orders have too much freedom and can distort the observed features. The results of these fits are given in column (2) of Table 6 where we list the simple means of the parameters derived from the 7 fits. The uncertainties quoted in the table are the quadratic sum of the internal uncertainties in a single fit and the standard deviation of the ensemble of 7 fits. In Figure 6 we show the best fitting model corresponding to the case with a 20-order Legendre normalizing function (thick solid curve). The polynomial itself is shown by the dotted line. The results from this particular fit are very close to the ensemble averages in Table 6.

The fit to the primary’s disentangled spectrum is very good. The results for T_{eff} , $[\text{m}/\text{H}]$, and the contribution factor are all consistent at the 1σ level with previous determinations (26,450 K, -0.63 , and 63.9%, respectively). The value of $\log g$ is 0.12 dex ($\sim 2.2\sigma$) higher than that determined from the binary analysis. However, this is not a large discrepancy and, since the gravity determination depends on the wings of the Balmer lines, we suspect it arises from deficiencies in the normalization of the original echelle spectra. It is interesting that the metallicity determined here — which mainly reflects weak but numerous lines of O II — agrees so well with that derived by the SED analysis — based mainly Fe II and III absorption in the UV. These two results present a very consistent picture of a general factor-of-4 metal underabundance for HV 5936. Note that all of the fits to the primary’s spectrum assume a helium abundance of $n(\text{He})/n(\text{H}) = 0.084$, which is based on the observed metal abundance and standard chemical enrichment laws (see §5) and corresponds to a helium mass fraction of $Y = 0.25$.

Fits to the secondary’s spectrum were performed in a similar manner as above except that — since the optical metal lines are all too weak to allow a meaningful determination of $[\text{m}/\text{H}]$ — we fixed its value to $[\text{m}/\text{H}] = -0.63$ as derived in §3. Also, we found that the 10-order Legendre fit was inadequate to model the continuum undulations and so we base our results on 6 fits with normalization polynomials of 15, 20, 25, 30, 35, and 40 orders. The resulting mean parameters and 1σ uncertainties from these fits are listed in column (3) of Table 6. These results are much less satisfying than for the primary. T_{eff} , $\log g$, and the contribution factor all differ greatly from the previously determined values (17,600 K, 3.49, and 36.1%, respectively). In addition, the value of $v \sin i$ appears inconsistent with the virtually unavoidable requirement that the secondary’s rotation be tidally locked to its orbit (see §5).

From detailed examination of the fits to the secondary, we found that the discrepancies arise essentially because the secondary’s He I lines are too strong to be well-fit with the tem-

perature of 17,600 K inferred earlier in §3. It is not likely, however, that the secondary can be significantly hotter than this, since this temperature results from a very well-determined eclipse-based temperature ratio and an apparently well-determined primary star temperature. Rather, we suggest that the secondary’s He I lines are enhanced in strength arising from a modest enhancement in the He surface abundance. The viability of this suggestion is demonstrated by Case II in column (4) of Table 6. The mean parameters and 1σ uncertainties were derived in an identical manner to those in Case I, except that the helium abundance was approximately doubled to a value of $n(\text{He})/n(\text{H}) = 0.16$. In addition, the abundances of C and O were depleted by a factor of 10, compared to the base metallicity of $[\text{m}/\text{H}] = -0.626$, and N was enhanced by a factor of 70. These factors are based on stellar interior models which will be discussed below in §5. It is clear that these adjustments to the elemental abundances yield results completely consistent with the previous measurements of T_{eff} and $\log g$ for the secondary and the known value of the continuum contribution factor. In addition the value of $v \sin i$ is well-determined and consistent with synchronous rotation (see §5). In Figure 7 we show the best-fitting model corresponding to Case II with a 25-order Legendre normalizing function (thick solid curve). The results from this particular fit are very close to the ensemble averages in column (4) Table 6.

The value of $n(\text{He})/n(\text{H})$ used in Case II was not arrived at arbitrarily. Rather, we ran a set of fits to the secondary’s spectrum (each with a different order Legendre polynomial) with T_{eff} held fixed at the value of 17,600 K found in §3 and with the He abundance as a free parameter. (T_{eff} and $n(\text{He})/n(\text{H})$ are degenerate in their effects and cannot both be determined from fitting the spectrum.) This set of models resulted in a best-fitting He abundance of $n(\text{He})/n(\text{H}) = 0.157 \pm 0.018$, which we rounded off to use in Case II. The significance of this result as an indicator of a true He enhancement can be gauged from a similar analysis of the primary. A set of fits of the primary’s spectrum, with T_{eff} fixed at 26,450 K (from the SED analysis) and the He abundance as a free parameter, yielded a best fitting He abundance of $n(\text{He})/n(\text{H}) = 0.090 \pm 0.007$. This is consistent with that inferred in §5 below, from the metallicity of the system and chemical enrichment laws.

Our conclusions from analysis of the high-resolution disentangled optical spectra of HV 5936 are twofold: 1) the primary’s absorption line spectrum is completely consistent with the stellar properties derived in §3, given the random errors and small systematic effects which may have arisen during the processing and “disentangling” of the spectra; and 2) the secondary’s spectrum is consistent with the derived properties only if a \sim factor-of-2 enhancement is assumed in the surface He abundance, as compared to that of the primary. In §5 below we consider the plausibility of a He enhancement in the secondary.

5. The History and Nature of the HV 5936 Binary System

We summarize the basic physical properties of the HV 5936 system in Table 7. The notes to the Table indicate how the individual stellar properties were derived from the results of the preceding sections. A scale model of the system is shown in Figure 8. The locations of the HV 5936 components in the $\log T_{\text{eff}}$ vs. $\log L$ diagram are shown in Figure 9, where the skewed rectangular boxes indicate the 1σ error loci (recall that errors in T_{eff} and L are correlated). The position of the Zero Age Main Sequence (ZAMS) is indicated in Figure 9 by the thick curve; the theoretical evolution tracks shown on the figure will be discussed below.

Examination of Figure 9 and Table 7 suggests a paradox, in that the more evolved star (i.e., farthest from the ZAMS) is the less massive component of the pair. The most plausible explanation for this scenario is that HV 5936 is a post-mass transfer system, as commonly argued to explain the so-called “Algol paradox.” The originally more massive star evolved beyond the Roche critical surface at a certain point and some fraction of its mass was transferred to its companion. After that process, the mass-accreting component became more massive than the mass-donor, and this is the current status of the system.

In contrast with our previous studies, the strong interaction between the system components prevents us from using evolutionary models to perform a critical self-consistency check of the results. I.e., a single isochrone is not expected to fit both components of the system because of their history of mass transfer. However, comparison with theoretical evolution tracks is still instructive. Thus, we considered the evolutionary models of Claret (1995, 1997) and Claret & Giménez (1995, 1998) (altogether referred to as the CG models). These models cover a wide range in both metallicity (Z) and initial helium abundance (Y), incorporate the most modern input physics, and use a value of $0.2 H_p$ as the convective overshooting parameter. In our particular case, we adopted the metal abundance from the SED fit (see Table 7), which results in a value of $Z = 0.005$. Using this metal abundance, the empirical chemical law of Ribas et al. (2000b) yields a helium abundance of $n(\text{He})/n(\text{H}) = 0.084$, corresponding to $Y = 0.25$. (The analysis of the disentangled spectrum of the primary in §4 provides a remarkable confirmation of this result.)

In Figure 9 we show the CG models for masses of $11.6 M_{\odot}$ and $4.7 M_{\odot}$, corresponding to the masses measured for the HV 5936 components. Despite its history of significant mass gain, the primary component has a luminosity in excellent agreement with theoretical expectations for a star of its mass and radius. This is not surprising since it has been shown that the hydrodynamical relaxation time of the accretion process is short enough so that the mass-gaining component in a non-conservative system is expected to behave like a normal star of its mass and radius (De Grève 1991, 1993). Empirical proof of this has been obtained

from the study of galactic Algol systems (García & Giménez 1990). The secondary, on the other hand, is significantly over-luminous for its current mass. This is consistent with the behavior exhibited by the mass-donors in galactic Algol systems (Giuricin, Mardirossian, & Mezzetti 1983; Hilditch & Bell 1987).

The rotational velocity determined from the disentangled spectrum for the secondary is consistent with synchronization with the orbit (compare the values of $v \sin i$ and v_{syn} in Table 7). This is expected since the secondary completely fills its Roche lobe and tidal forces are very efficient at locking the star’s spin rate to follow the orbital motion. This agreement between observations and theoretical expectations provides a consistency check on the measurements of $v \sin i$, stellar radius, and orbital properties. The primary component, however, is seen to have a rotational velocity that is $\sim 25\%$ larger than the synchronization value. The departure from unity is well beyond the observational uncertainties — but is not unprecedented or unexpected. The primaries of numerous galactic Algol systems have been determined to rotate faster than their synchronous rate and even close to the centrifugal limit (see, e.g., van Hamme & Wilson 1990). A rotational velocity 25% larger than synchronicity is well within the observed range. Angular momentum transfer through mass accretion is probably the most plausible model to explain the spin-up of Algol primaries (Huang 1966).

The \sim factor-of-2 enhancement observed in the secondary’s surface He abundance, as discussed in §4, provides a strong constraint on the original masses of the stars in the HV 5936 system, particularly the secondary. The nature of this constraint is as follows: the initial mass of the current secondary must have been such that, by the time the star evolved to fill its Roche Lobe (and commence mass transfer), the point in its interior where the He abundance was twice the surface value was at a radius which enclosed $4.7 M_{\odot}$ of material (i.e., the current mass of the secondary). This interior point — now at the surface of the secondary — clearly must have been in the outer regions of its original H-burning core.

To exploit this constraint, we considered the evolution of 4 different simulated binary systems, constructed with the assumptions of: 1) non-conservative mass exchange with 50% efficiency in the transfer of mass from the donor star to the mass gaining star and 2) a fractional angular momentum loss proportional to the fractional mass lost to the system. The initial masses of these systems were $12 M_{\odot}$ (current secondary) + $8 M_{\odot}$ (current primary), $14 M_{\odot}$ + $7 M_{\odot}$, $16 M_{\odot}$ + $6 M_{\odot}$, and $18 M_{\odot}$ + $5 M_{\odot}$. The calculations were done following the formalism in Torres, Neuhäuser, & Wichmann (1998) but considering the non-conservative mass transfer expression in Vanbeveren et al. (1979). From these, we estimate initial orbital periods of 1.154, 1.318, 1.689, and 2.449 days, and initial Roche lobe radii of 4.8, 5.2, 6.1, 7.8, and 10.7 R_{\odot} , respectively, for the four mass combinations. The results showed that each of the systems experiences Case A mass transfer (i.e., occurring during

the core hydrogen burning phase of the mass donor) and all could eventually evolve to the configuration observed for HV 5936 — but with different resultant surface He abundances for the mass donor. Using internal composition profiles computed by one of us (A.C.), we find that the surface He abundances of the initially $12 M_{\odot}$, $14 M_{\odot}$, $16 M_{\odot}$, and $18 M_{\odot}$ mass donors are enhanced by factors of 1.5, 2.6, 3.0, and 3.5, respectively, by the time donor has been reduced to $4.7 M_{\odot}$. The observed enhancement of ~ 2.0 is roughly midway between the $12 M_{\odot}$ and $14 M_{\odot}$ cases.

Taking into account all the results above, we postulate that the HV 5936 system began with initial masses of $\sim 13 M_{\odot}$ and $\sim 7.5 M_{\odot}$ for the current secondary and current primary, respectively. Case A mass exchange then resulted in the observed current masses of the components, the spinning up of the primary to a rotational rate faster than the synchronous rate, and the uncovering of processed material in the atmosphere of the secondary. The estimated initial mass of the secondary depends only weakly on our assumption of a 50% mass transfer efficiency (which is probably an upper limit). The primary’s initial mass is much more sensitive to this assumption, although it might be possible to constrain it further (and thus the transfer efficiency) by considering the spin-up process. Along with the He enhancement, the secondary’s surface should also exhibit a $\sim 70\times$ enhancement of ^{14}N and a $\sim 10\times$ depletion of ^{12}C and ^{16}O , according to our interior composition models. These enhancements and depletions were assumed in the Case II modeling of the secondary’s disentangled spectrum as discussed in §4 above. Because of the already low metallicity of this LMC star, the modifications in CNO abundances do not have striking effect on the secondary’s spectrum. In Figure 7 we indicate the locations of the most prominent N II lines. Even with their enhanced abundances, these lines are too weak to claim a positive detection, although there do appear to be features in the spectrum at their locations. Higher quality spectra will be required to confirm their presence and, thus, the surface enhancement of N.

6. The Interstellar Medium Towards HV 5936

Our analysis of HV 5936 provides some insight into the conditions of the interstellar medium along the line of sight to the system. In this section we examine this information and also show how these data help constrain the relative position of HV 5936 within the LMC.

The column density of interstellar H I in the foreground of HV 5936 was measured by comparing the observed H I Ly α 1216.7 Å absorption line profile (using the unbinned FOS data) with theoretical profiles consisting of a synthetic stellar spectrum convolved with an

interstellar absorption profile. In general, the interstellar profile is constructed by assuming a component at 0 km s^{-1} with $N(\text{H I}) = 5.5 \times 10^{20} \text{ cm}^{-2}$, corresponding to Milky Way foreground gas (see, e.g., Schwering & Israel 1991), and a second component with a LMC-like velocity and a column density which is varied to produce the best fit to the data (as judged by visual inspection).

In examining the FOS data for HV 5936, we found no evidence for H I absorption at LMC velocities, and a Milky Way contribution at 0 km s^{-1} of $5.0 \times 10^{20} \text{ cm}^{-2}$, slightly less than, but consistent with, the mean value of Schwering & Israel. The best-fitting Ly α profile is shown in Figure 10, where we illustrate the unbinned FOS spectrum, the synthetic stellar spectrum (dotted line) and the convolution of the synthetic spectrum with the interstellar profile (thick solid curve). Note that the bottom of the Ly α profile is filled in by geocoronal emission.

This notable absence of neutral LMC interstellar gas towards HV 5936 is consistent with the interstellar reddening results. The value of $E(B - V) = 0.047 \pm 0.004 \text{ mag}$ found for HV 5936 from the SED analysis is essentially identical to the mean value for 56 Milky Way foreground stars within 1° of the HV 5936 line-of-sight ($E(B - V) = 0.048$ from the data of Oestreich, Gochermann, & Schmidt-Kaler 1995). Thus, there is no measurable contribution to $E(B - V)$ from LMC material.

The lack of large amounts of LMC gas and dust towards HV 5936 provides an opportunity to examine some properties of the Milky Way ISM along a sightline passing completely through the Milky Way’s halo — but free of extragalactic contamination. In particular, the gas-to-dust ratio for this material is $N(\text{H I})/E(B-V) = 1 \times 10^{22} \text{ cm}^{-2} \text{ mag}^{-1}$, which is roughly twice the value found in the Galactic disk and suggests a “cleaner” ISM in the halo. In addition, the wavelength-dependent extinction curve derived from the SED analysis is now recognized to be a measure of the extinction properties of Galactic halo dust grains. This curve is shown in Figure 11 where the small symbols indicate the normalized ratio of model fluxes to observed fluxes, while the thick solid line shows the parameterized representation of the extinction curve, which was actually determined by the fitting process. The most remarkable feature of this curve is the very weak 2175 Å bump, which may be the weakest bump ever seen in Milky Way dust. The curve is consistent with the results of Kizskurno-Koziej & Lequeux (1987), which show a weak trend of weakening bump strength and steepening 1500–1800 Å extinction with increasing height above the Galactic plane. The shape of the HV 5936 curve is very similar to those seen towards HV 982 and EROS 1044 (Papers II and III), whose total extinctions are dominated by Milky Way dust.

The ISM results for HV 5936 provide constraints on the position of the system within the LMC. Its apparent location places it within the outlines of LMC-4, the largest supergiant

H II shell in the LMC (Goudis & Meaburn 1978; Meaburn 1980). The shell has a diameter of ~ 1.1 kpc, and HV 5936 is positioned NE of the shell center and near the inside edge. A hint of the shell can be seen in Figure 1. The position of the shell coincides with a “hole” in the H I distribution (McGee & Milton 1966). The H I 21-cm emission line data of Rohlfs et al. (1984), obtained with a half-power beam width of $15'$, reveal a total LMC H I column density of $2.4 \times 10^{20} \text{cm}^{-2}$ at the position of HV 5936, with higher values to the east and comparable values in other directions. The minimum value of $N(\text{H I})$ seen in the general vicinity of HV 5936 is $1.6 \times 10^{20} \text{cm}^{-2}$, at a position $0.4'$ west of the system. While we have not established a rigorous upper limit for the non-detection of LMC H I Ly α absorption towards HV 5936, such a limit is certainly below 10^{20}cm^{-2} . Thus, while we cannot rule out the presence of localized, deep holes in the ISM distribution, the simplest explanation of both the HV 5936 gas and dust results is that the system lies at an undetermined distance above the main H I layer at its apparent location on the LMC.

7. The Distance to HV 5936

The discussion in §5 demonstrates that, despite the interesting evolutionary state of the HV 5936 system and the mass exchange that has occurred, the stellar properties appear well-determined and well-understood. Particularly, the properties of the primary star are indistinguishable from those of a “normal” single star, which came by its mass through the normal star-formation process. We can thus determine a distance to the system based on the results for the primary star, by combining its absolute radius R_P (derived from the classical EB analysis) with the distance attenuation factor $(R_P/d)^2$ (derived from the SED analysis). We find $d_{\text{HV5936}} = 43.2 \pm 1.8$ kpc, corresponding to a distance modulus of $(V_0 - M_V)_{\text{HV5936}} = 18.18 \pm 0.09$ mag.

The uncertainty in the distance is estimated from considering three independent sources of error: (1) the internal measurement errors in R_P and $(R_P/d)^2$ as given in Table 3; (2) uncertainty in the appropriate value of the extinction parameter $R(V)$; and (3) uncertainty in the FOS flux scale zeropoint due to calibration errors and instrument stability. Straightforward propagation of errors shows that these three factors yield individual uncertainties of ± 1.7 kpc, ± 0.3 kpc (assuming $\sigma R(V) = \pm 0.3$), and ± 0.4 kpc (assuming $\sigma f(\text{FOS}) = \pm 2.5\%$), respectively. The overall 1σ uncertainty quoted above is the quadratic sum of these three errors. It is dominated by the uncertainty in the primary’s radius, which alone accounts for 1.7 kpc in the error budget. Note that the only “adjustable” factor in the analysis is the extinction parameter $R(V)$, for which we have assumed the value 3.1. Because of the very low reddening of the system, our distance result is very insensitive to this assumption. The weak dependence

of the distance modulus on $R(V)$ is given by: $(V_0 - M_V)_{\text{HV5936}} = 18.18 - 0.04 \times [R(V) - 3.1]$.

We have considered the possibility that this distance result may be tainted due to the advanced evolutionary state of the secondary star. In general, the light curve and radial velocity curve analyses are very insensitive to the natures of the EB’s components, i.e., the temperature ratio of the two stars, their mean radii, surface gravities, and relative contributions to the observed light in the optical spectral region are virtually model-independent and very well-determined. These results tightly constrain the SED analysis and so it would seem that the results could be compromised only if the secondary’s SED departs significantly from the shape predicted by an ATLAS9 model of the derived T_{eff} , $\log g$, $[\text{m}/\text{H}]$, and v_{micro} values. The evidence, however, suggests that this is not the case. In support, we note the high quality of the fit to the combined SED of the system, which is comparable to our previous studies of systems containing wholly “normal” stars, and the consistency between the SED analysis and the independent modeling of the disentangled optical spectra (see §4). The only anomaly found is the probable modest enhancement of the secondary’s He abundance, which would have only very small effect on the star’s SED. We have run a number of tests with the SED analysis, arbitrarily modifying the secondary’s SED (by varying T_{eff} , $\log g$, $[\text{m}/\text{H}]$, or v_{micro}). Even relatively large changes have little effect on the derived system distance, because of the dominance of the primary in the combined SED. We thus conclude, based both on a lack of contrary evidence and on the apparent robustness of the result, that uncertainties arising from the evolutionary state of the secondary are likely significantly smaller than the other sources of error noted above.

In Table 8 we show the individual system distances for HV 5936 and the other EBs in our study. We also list the implied distances to a standard reference point in the LMC, based on the assumption that the EBs are all located within a flat disk-like LMC whose spatial orientation is specified by an inclination angle and a position angle for the line of nodes in the plane of the sky. We choose the optical center of the LMC’s Bar as the reference point and show two sets of LMC distances, based on two different assumptions about the LMC’s spatial orientation. Details are given in the Notes to the Table.

The results for HV 5936 in Table 8 clearly stand out from the others. This is partially explained by projection effects. Because HV 5936 lies relatively far from the adopted reference point and in the “nearside” of the LMC, it is expected to be somewhat closer than the other systems. However, when the projection is taken into account, the distance implied for the LMC reference point is 44.3 ± 1.8 kpc, corresponding to a distance modulus of 18.23 ± 0.09 (from taking a simple mean of the two cases shown in Table 8). This is about 2σ away from the mean of the other systems and suggests that the assumption that all the systems lie in the same flat disk may be invalid.

Although the relatively large uncertainty in the HV 5936 result prevents definitive conclusions, we suggest that HV 5936 lies “above” the extrapolated position of the LMC’s disk. This notion is consistent with, and actually suggested by, the interstellar results, which reveal no evidence for absorption by LMC H I and no measurable extinction by LMC dust along the HV 5936 sightline. This interpretation of the ISM data is complicated by the coincidence of HV 5936’s position in the sky with the supergiant shell LMC 4, towards which a very low H I 21-cm emission column density is observed. Depending on the patchiness of the H I, it is conceivable that a star located within or even behind LMC 4 could show an undetectably low H I absorption column density. This seems unlikely for HV 5936, however, since it is located near the eastern edge of the LMC 4, where the 21-cm column density is $\sim 2.4 \times 10^{20} \text{ cm}^{-2}$ and rises steeply towards the east. The simplest explanation is that HV 5936 just lies in front of most of the LMC’s interstellar matter. It is not clear why HV 5936 should occupy such a position, although this might well be related to the formation of shell LMC 4 itself. Likewise, it remains to be seen whether HV 5936 is a pathological object, in terms of its location, or is merely representative of a spatially extended stellar population in the NE quadrant of the LMC.

Alternative explanations for the HV 5936 results include assuming simple error in the spatial orientation of the LMC or perhaps a major structural feature, such as a warp, in the LMC’s disk. The latter may arise from strong past interactions between the Magellanic Clouds and the Milky Way galaxy. Both hypotheses would allow HV 5936 to lie close to the LMC’s disk (but still above, given the ISM results), but require the disk to be closer to us than currently assumed. Unfortunately for these ideas, the required orientation for the LMC would necessitate an inclination angle ($\sim 60^\circ$) much steeper than previously measured. Moreover, structural studies of the LMC have revealed no evidence of a warp in the vicinity of HV 5936 (e.g., see Olsen & Salyk 2002).

8. Final Comments

The analysis presented here for HV 5936 has differed somewhat from those reported previously in Papers I, II, and III. Here our efforts have been focused more strongly on the physical properties of the stellar components and the evolutionary history of the binary system, rather than on the distance measurement. This arises from the interesting evolutionary state of this semidetached system and from its outlying location in the LMC. Because of its location, the implications of HV 5936’s individual distance for the distance to the LMC as a whole is not as firmly established as for our previously analyzed systems.

It is worth noting that HV 5936 is the first semidetached EB system to be used as a dis-

tance indicator for the LMC. Although our current analysis shows that semidetached binaries can be used successfully as such, there are a number of complications that call for the careful use of these systems. Among the related problems are: 1) The lack of evolutionary cross checks, 2) the often very unequal component masses, effective temperatures and luminosities that complicate the spectrophotometric analysis, 3) the large out-of-eclipse variations and distortions, and 4) the relative radii that are strongly dependent on the adopted mass ratio. Our success with HV 5936 springs directly from the high quality observations available, in which the spectroscopic and photometric signatures of both stars are clearly present and separable.

Future distance studies within our program will be focused primarily on non-interacting systems lying closer to the apparent center of the LMC. We currently have four detached systems under analysis, all of which can be expected to yield accurate distances and a number of cross checks to verify the results. In addition, two of these systems, EROS 1066 and MACHO 053648.7–691700 (see Figure 1), have been especially selected to provide insight into the possible problem of line-of-sight extension of the LMC.

This work was supported by NASA grants NAG5-7113, HST GO-06683, HST GO-08691, and NSF/RUI AST-0071260. We are grateful for the skilled assistance of the CTIO support staff during our observing runs. E.F. acknowledges support from NASA ADP grant NAG5-7117 to Villanova University and thanks Michael Oestreicher for kindly making his LMC foreground extinction data available.

REFERENCES

- Albright, G. E., & Richards, M. T. 1993, *ApJ*, 414, 830
- Balachandran, S., Lambert, D. L., Tomkin, J., & Parthasarathy, M. 1986, *MNRAS*, 219, 479
- Bell, S. A., Hill, G., Hilditch, R. W., Clausen, J. V., & Reynolds, A. P. 1993, *MNRAS*, 265, 1047
- Claret, A. 1995, *A&AS*, 109, 441
- Claret, A. 1997, *A&AS*, 125, 439
- Claret, A., & Giménez, A. 1995, *A&AS*, 114, 549
- Claret, A., & Giménez, A. 1998, *A&AS*, 133, 12

- De Grève, J. P. 1991, in IAU Symposium No. 151, Evolutionary Processes in Interacting Binary Stars, eds. Y. Kondo, R. F. Sistero, & R. S. Polidan (Dordrecht: Kluwer), 41
- De Grève, J. P. 1993, *A&AS*, 97, 527
- Fitzpatrick, E. L. 1986, *AJ*, 92, 1068
- Fitzpatrick, E. L. 1999, *PASP*, 111, 63
- Fitzpatrick, E. L., & Massa, D. 1990, *ApJS*, 72, 163
- Fitzpatrick, E. L., Ribas, I., Guinan, E. F., DeWarf, L. E., Maloney, F. P., & Massa, D. 2002, *ApJ*, 564, 260 (Paper II)
- García, J. M., & Giménez, A. 1990, *Ap&SS*, 169, 121
- Giuricin, G., Mardirossian, F., & Mezzetti, M. 1983, *ApJS*, 52, 35
- Goudis, C., & Meaburn, J. 1978, *A&A*, 68, 189
- Guinan, E. F., et al. 1998, *ApJ*, 509, L21 (Paper I)
- Hadrava, P. 1995, *A&AS*, 114, 393
- Hadrava, P. 1997, *A&AS*, 122, 581
- Hilditch, R. W., & Bell, S. A. 1987, *MNRAS*, 229, 52
- Huang, S.-S. 1966, *AJ*, 71, 165
- Isserstedt, J. 1975, *A&A*, 41, 21
- Jensen, K. S., Clausen, J. V., & Giménez, A. 1988, *A&AS*, 74, 331
- Kiszkurno-Koziej, E., & Lequeux, J. 1987, *A&A*, 185, 291
- Klinglesmith, D. A., & Sobieski, S. 1970, *AJ*, 75, 175
- Koornneef, J. 1982, *A&A*, 107, 247
- Lubow, S. H., & Shu, F. H. 1975, *ApJ*, 198, 383
- McGee, R. X., & Milton, J. A. 1966, *Australian J. Phys.*, 19, 343
- Meaburn, J. 1980, *MNRAS*, 192, 365
- Meurs, E. J. A., & van den Heuvel, E. P. J. 1989, *A&A*, 226, 88

- Milone, E. F., Stagg, C. R., & Kurucz, R. L. 1992, *ApJS*, 79, 123
- Morgan, D. H., & Nandy, K. 1982, *MNRAS*, 199, 979
- Mould, J. R., et al. 2000, *ApJ*, 529, 786
- Oestreicher, M. O., Gochermann, J., & Schmidt-Kaler, T. 1995, *A&AS*, 112, 495
- Olsen, K. A. G., & Salyk, C. 2002, *AJ*, in press (astro-ph/0207077)
- Ribas, I., et al. 2000a, *ApJ*, 528, 692
- Ribas, I., Jordi, C., Torra, J., & Giménez, A. 2000b, *MNRAS*, 313, 99
- Ribas, I., Fitzpatrick, E. L., Maloney, F. P., Guinan, E. F., & Udalski, A. 2002, *ApJ*, 574, 771 (Paper III)
- Rohlfs, K., Kreitschmann, J., Siegman, B. C., & Feitzinger, J. V. 1984, *A&A*, 137, 343
- Schmidt-Kaler, T., & Gochermann, J. 1992, in *ASP Conf. Ser. 30, Variable Stars and Galaxies*, ed. B. Warner (San Francisco: ASP), 203
- Schwering, P. B. W., & Israel, F. P. 1991, *A&A*, 246, 231
- Torres, G., Neuhäuser, R., & Wichmann, R. 1998, *AJ*, 115, 2028
- van der Marel, R. P. & Cioni, M.-R. L. 2001, *AJ*, 122, 1807
- van Hamme, W., & Wilson, R. E. 1990, *AJ*, 100, 1981
- Vanbeveren, D., De Grève, J. P., van Dessel, E. L., & de Loore, C. 1979, *A&A*, 73, 19
- Wilson, R. E., & Devinney, E. J. 1971, *ApJ*, 166, 605 (W-D)

Table 1. HST Spectrophotometric Observations of HV 5936

Instrument	Detector	Dataset Name	Date of Observation	Orbital Phase	k_P^a	k_S^a
FOS	G130H	Y3FU0803T	31 Jan 1997	0.115	1.0059	0.9875
FOS	G190H	Y3FU0806T	31 Jan 1997	0.137	1.0116	1.0151
FOS	G270H	Y3FU0805T	31 Jan 1997	0.133	1.0106	1.0101
FOS	G400H	Y3FU0804T	31 Jan 1997	0.128	1.0093	1.0038
STIS	G430L	O665B6030	22 April 2001	0.654	1.0491	1.0360
STIS	G750L	O665B6040	22 April 2001	0.657	1.0490	1.0396

^aThe quantities k_P and k_S are corrections used in the spectral energy distribution analysis to account for out-of-eclipse light variations in the HV 5936 system, due to reflection effects and gravitational distortion of the secondary. See §3.3.

Table 2. Heliocentric Radial Velocity Measurements for HV 5936

HJD (−2400000)	Orbital Phase	RV_P (km s^{-1})	RV_S (km s^{-1})	$(O-C)_P$ (km s^{-1})	$(O-C)_S$ (km s^{-1})
51558.7339	0.6719	411.2	84.6	1.8	2.0
51558.7600	0.6812	413.7	77.5	1.5	1.3
51560.7402	0.3871	240.4	486.6	−1.9	−6.2
51560.7659	0.3963	246.8	475.4	−0.3	−5.8
51561.6849	0.7239	421.1	55.8	−0.2	−1.1
51561.7072	0.7318	421.6	53.5	−0.5	−1.6
51562.7743	0.1122	245.7	484.5	1.3	1.0
51562.7930	0.1189	240.6	490.5	−0.3	−1.2
51895.7673	0.8234	412.8	76.3	0.2	−1.3
51895.7906	0.8317	408.4	81.2	−1.6	−2.4
51898.6384	0.8470	402.7	96.0	−1.9	0.0
51898.6616	0.8553	402.7	102.1	1.3	−1.6
51899.6325	0.2014	211.9	565.6	1.1	2.8
51899.7847	0.2556	206.5	578.1	1.0	3.0
51900.8064	0.6199	387.3	133.8	−0.3	1.3
51900.8296	0.6281	391.9	127.4	0.2	4.5
51902.6812	0.2882	207.6	569.7	−0.7	0.4
51902.7046	0.2966	209.6	568.0	−0.2	1.8

Table 3. Results From Light Curve, Radial Velocity Curve, and Spectrophotometry Analyses

Parameter	Value
<i>Light Curve Analysis</i>	
Period	2.8050681 ± 0.0000015 days
Eccentricity	0.0 (fixed)
Inclination	80.0 ± 0.2 deg
$T_{\text{eff}}^{\text{S}}/T_{\text{eff}}^{\text{P}}$	0.666 ± 0.008
$[L_{\text{S}}/L_{\text{P}}]_{\text{B}}$	0.592 ± 0.011
$[L_{\text{S}}/L_{\text{P}}]_{\text{V}}$	0.629 ± 0.012
r_{P}^{a}	0.2708 ± 0.0088
r_{S}^{a}	0.3053 ± 0.0034
$\Omega_{\text{P}}^{\text{b}}$	4.14 ± 0.15
$\Omega_{\text{S}}^{\text{b}}$	2.69 ± 0.04
$\Delta\phi$	0.0006 ± 0.0005
<i>Radial Velocity Curve Analysis</i>	
K_{P}	109.1 ± 3.2 km s ⁻¹
K_{S}	268.2 ± 7.5 km s ⁻¹
q^{c}	0.407 ± 0.016
v_{γ}	314.3 ± 5.8 km s ⁻¹
a	21.23 ± 0.46 R _⊙
<i>Energy Distribution Analysis</i>	
$T_{\text{eff}}^{\text{P}}$	$26,450 \pm 250$ K
$[\text{m}/\text{H}]_{\text{PS}}$	-0.63 ± 0.05
$v_{\text{micro}}^{\text{PS}}$	2.6 ± 0.6 km s ⁻¹
E(B–V)	0.047 ± 0.005 mag
$\log(R_{\text{P}}/d)^2$	-23.046 ± 0.006

^aFractional stellar radius $r \equiv R/a$, where R is the stellar “volume radius” and a is the orbital semi-major axis.

^bNormalized potential at stellar surface.

^cMass ratio $M_{\text{S}}/M_{\text{P}}$.

Table 4. Offsets Applied to HST/STIS Observations of HV 5936

STIS Detector	Dataset Name	Offset (FOS – STIS)
G430L	O665B6030	$+10.2 \pm 0.5\%$
G750L	O665B6040	$+5.9 \pm 0.7\%$

Table 5. Extinction Curve Parameters for HV 5936

Parameter	Description	Value
x_0	UV bump centroid	$4.55 \pm 0.03 \mu\text{m}^{-1}$
γ	UV bump FWHM	$0.59 \pm 0.18 \mu\text{m}^{-1}$
c_1	linear offset	-1.01 ± 0.40
c_2	linear slope	1.02 ± 0.10
c_3	UV bump strength	0.53 ± 0.26
c_4	FUV curvature	0.61 ± 0.12
$R(V)$	A(V)/E(B – V)	3.1 (assumed)

Note. — The extinction curve parametrization scheme is based on the work of Fitzpatrick & Massa 1990 and the complete UV-through-IR curve is constructed following the recipe of Fitzpatrick 1999.

Table 6. Analysis of Disentangled Spectra of HV 5936 Components

Stellar Property	Primary	Secondary	Secondary
(1)	(2)	Case I	Case II
(1)	(2)	(3)	(4)
$n(\text{He})/n(\text{H})$	0.084 ^a	0.084 ^a	0.16 ^b
T_{eff} (K)	$26,900 \pm 370$	$21,040 \pm 590$	$17,620 \pm 250$
$\log g$ (cgs)	4.11 ± 0.04	3.73 ± 0.10	3.54 ± 0.06
$[\text{m}/\text{H}]$	-0.60 ± 0.04	-0.63^{c}	-0.63^{c}
v_{micro} (km s ⁻¹)	2.6 ^d	2.6 ^d	2.6 ^d
$v \sin i$ (km s ⁻¹)	127.8 ± 1.6	139.0 ± 5.4	127.0 ± 2.2
v_{radial} (km s ⁻¹)	314.5 ± 1.2	318.0 ± 1.8	316.7 ± 1.7
contribution to light (%)	$62.3 \pm 1.3^{\text{e}}$	$40.5 \pm 1.2^{\text{e}}$	$36.7 \pm 0.4^{\text{e}}$

^aAssumed, from the discussion in §5; corresponds to $Y = 0.25$.

^bEnhanced He abundance. Also the abundances of C, N, and O, were adjusted by factors of 0.1, 70, and 0.1, respectively relative to the base metallicity of $[\text{m}/\text{H}] = -0.63$. See the discussions in §4 and 5.

^cThere are insufficient spectral features to measure $[\text{m}/\text{H}]$ from the optical spectrum of the secondary. The value of $[\text{m}/\text{H}]$ derived from the SED analysis in §3.3 is assumed.

^dThe microturbulence velocity cannot be measured with the existing data. The value derived from the SED analysis in §3.3 is assumed.

^eContribution factors for the primary and secondary stars were determined independently of each other. They were not constrained to add up to 100%.

Table 7. Physical Properties of the HV 5936 System

Property	Primary Star	Secondary Star
Spectral Type ^a	B0.5 V	B2 III
Mass ^b (M_{\odot})	11.6 ± 0.5	4.7 ± 0.2
Radius ^c (R_{\odot})	5.75 ± 0.23	6.48 ± 0.16
$\log g^d$ (cgs)	3.984 ± 0.039	3.488 ± 0.029
T_{eff}^e (K)	$26,450 \pm 250$	$17,600 \pm 330$
$\log(L/L_{\odot})^f$	3.98 ± 0.04	3.49 ± 0.03
[m/H] ^g	-0.62 ± 0.05	-0.62 ± 0.05
$n(\text{He})/n(\text{H})^h$	0.084	0.16
$v \sin i^i$ (km s^{-1})	127.8 ± 1.6	127.0 ± 2.2
$v_{\text{sync}} \sin i^j$ (km s^{-1})	103.1 ± 4.1	123.9 ± 2.9
d_{HV5936}^k (kpc)	43.2 ± 1.8	

^aEstimated from T_{eff} and $\log g$

^bFrom the mass ratio q and the application of Kepler’s Third Law.

^cComputed from the relative radii r_P and r_S and the orbital semimajor axis a .

^dComputed from $g = GM/R^2$.

^eDirect result of the spectrophotometry analysis and photometrically-determined temperature ratio.

^fComputed from $L = 4\pi R^2 \sigma T_{\text{eff}}^4$.

^gMean result from the SED analysis in §3.3 and the synthetic spectrum analysis for the primary in §5. For the secondary, abundance anomalies in CNO abundances would be expected, given the observed He enhancement.

^hFor the primary, this corresponds to a He mass fraction of $Y = 0.25$ and is based on the observed metallicity and standard chemical enrichment. See §5. For the secondary, $n(\text{He})/n(\text{H})$ is based on analysis of optical spectra in §4. The He enhancement is likely accompanied by modifications in the surface abundances of CNO. See §5.

ⁱ $v \sin i$ measured from the “disentangled spectra” of the two components as described in the text in §5.

^jTheoretical synchronization velocities.

^kUsing $(R_P/d)^2$ from the spectrophotometry analysis and R_P from the light curve and radial velocity curve analyses. See §7.

Table 8. Distances to LMC EB Systems

EB System	Reference	d_{EB}	d_{LMC} (Case I) ^a	d_{LMC} (Case II) ^b
HV 2274	Paper I,II	47.0 ± 2.2 kpc	45.9 kpc	47.0 kpc
HV 982	Paper II	50.2 ± 1.2 kpc	50.6 kpc	50.7 kpc
EROS 1044	Paper III	47.5 ± 1.8 kpc	47.3 kpc	47.4 kpc
HV 5936	This Paper	43.2 ± 1.8 kpc	44.0 kpc	44.7 kpc

^aDistance at a reference point at $(\alpha, \delta)_{1950} = (5^h24^m, -69^\circ47')$, corresponding to the optical center of the LMC’s bar according to Isserstedt 1975. Adopted LMC orientation defined by an inclination angle of 38° and a line-of-nodes position angle of 168° , from Schmidt-Kaler & Gochermann 1992. This orientation is illustrated in Figure 1.

^bDistance referred to the same reference point as above. Adopted LMC orientation defined by an inclination angle of $34^\circ.7$ and a line-of-nodes position angle of $122^\circ.5$, from van der Marel & Cioni 2001. In this case, the line of nodes runs approximately parallel to the long axis of the LMC’s Bar.

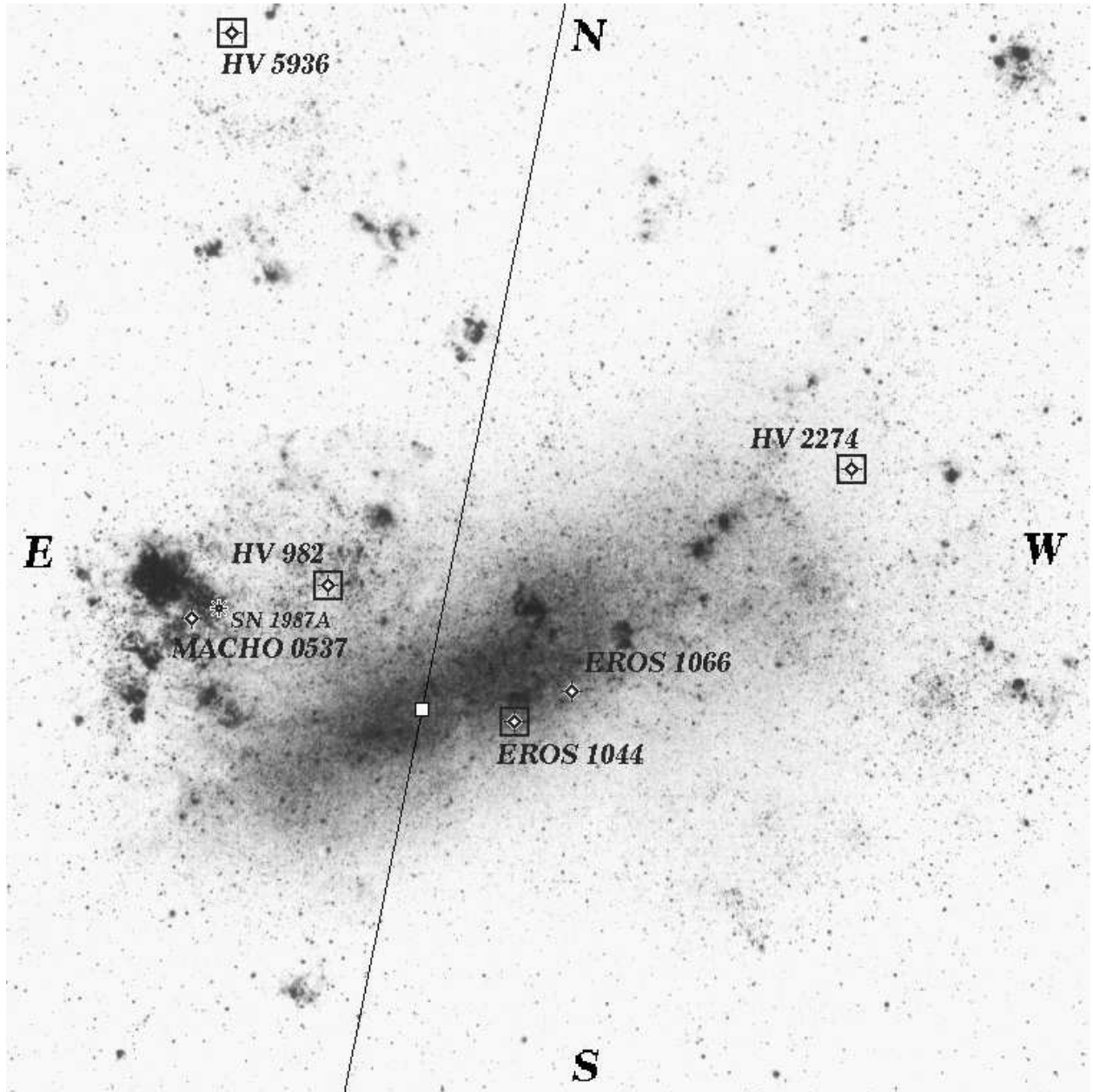


Fig. 1.— A photo of the Large Magellanic Cloud indicating the locations of HV 5936 (this paper), HV 2274 (Paper I), HV 982 (Paper II), EROS 1044 (Paper III) and two targets of future analyses, EROS 1066 and MACHO 053648.7-691700 (labeled in the figure as MACHO 0537). The optical center of the LMC’s bar according to Isserstedt 1975 is indicated by the open box and the LMC’s line of nodes, according to Schmidt-Kaler & Goehermann 1992, is shown by the solid line. The “nearside” of the LMC is to the east of the line of nodes. The location of SN 1987A is also indicated. Photo reproduced by permission of the Carnegie Institution of Washington.

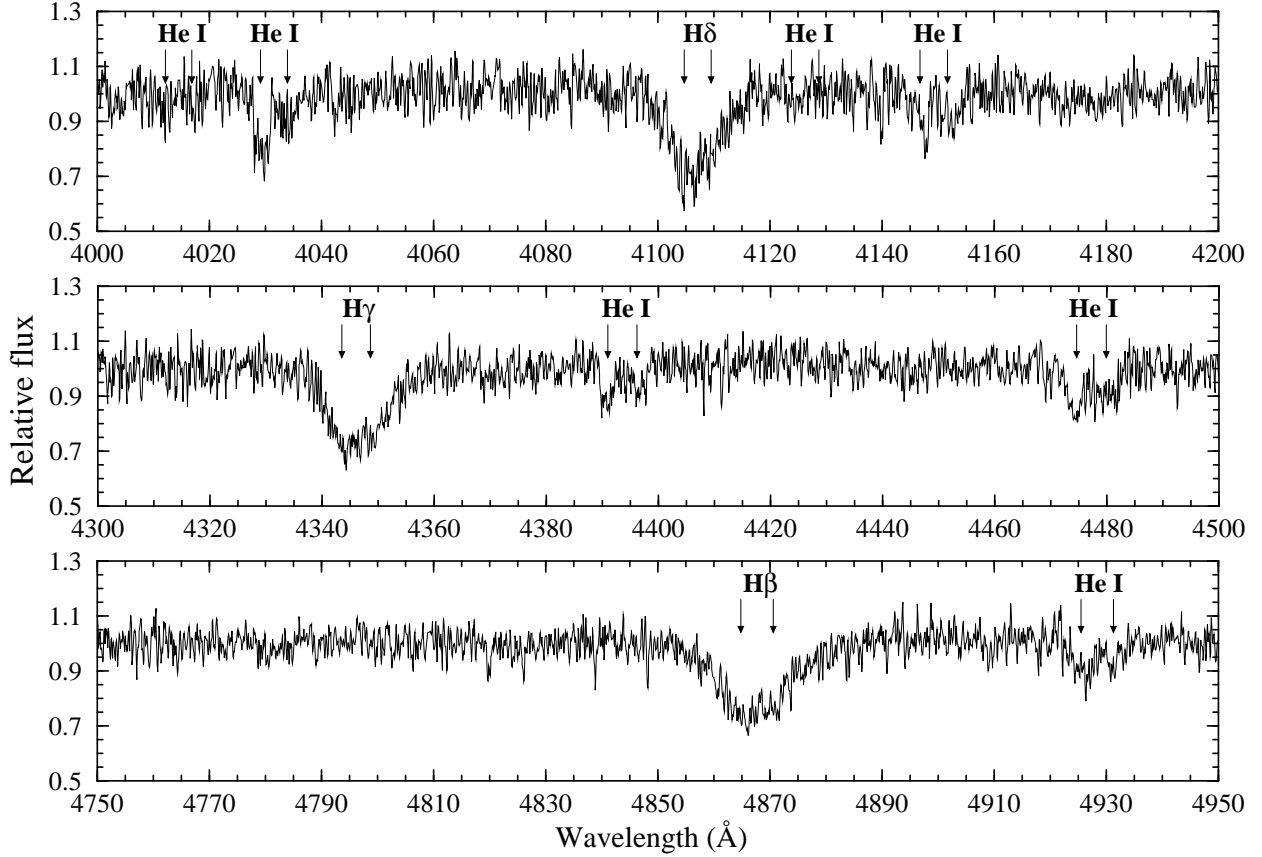


Fig. 2.— Normalized spectrum of HV 5936 near prominent H I and He I lines. The spectrum was obtained with the Blanco 4-m telescope at Cerro Tololo Inter-American Observatory on HJD 2451902.7046 at binary phase 0.297. The velocity separation between the primary and secondary stars at this phase is $\Delta v = 355 \text{ km s}^{-1}$. This figure demonstrates that the absorption lines from the two stars are cleanly resolved and, thus, that the radial velocity measurements will be immune to blending effects.

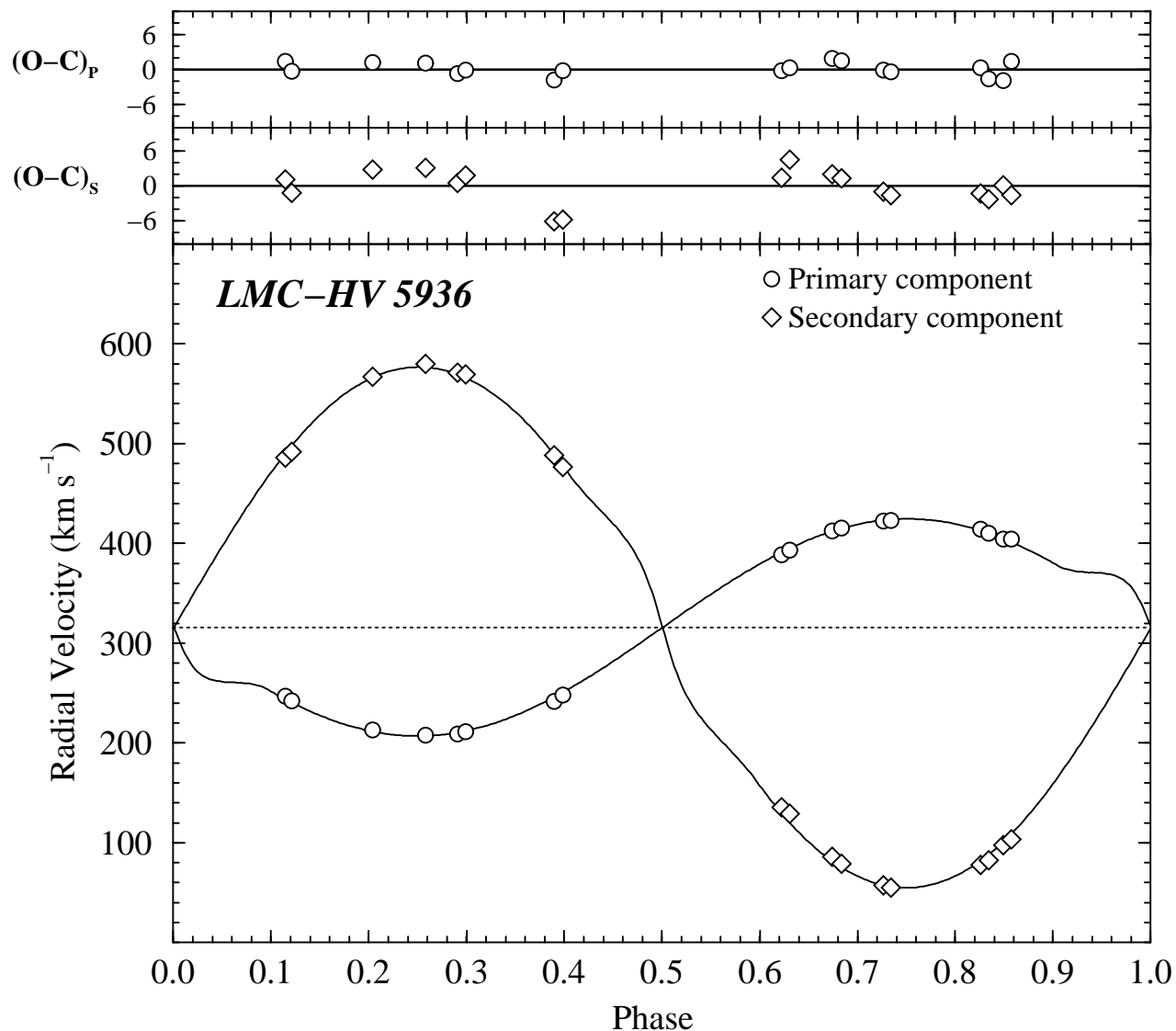


Fig. 3.— Radial velocity data for HV 5936 (see Table 1) superimposed with best-fitting model. The parameters derived from the data are listed in Table 2. Note that the details of the model curve, including the sharp discontinuity due to the partial eclipse of a rotating star (the Rossiter Effect), are not a product of the radial velocity curve analysis. The residuals to the fit are shown in the upper panel.

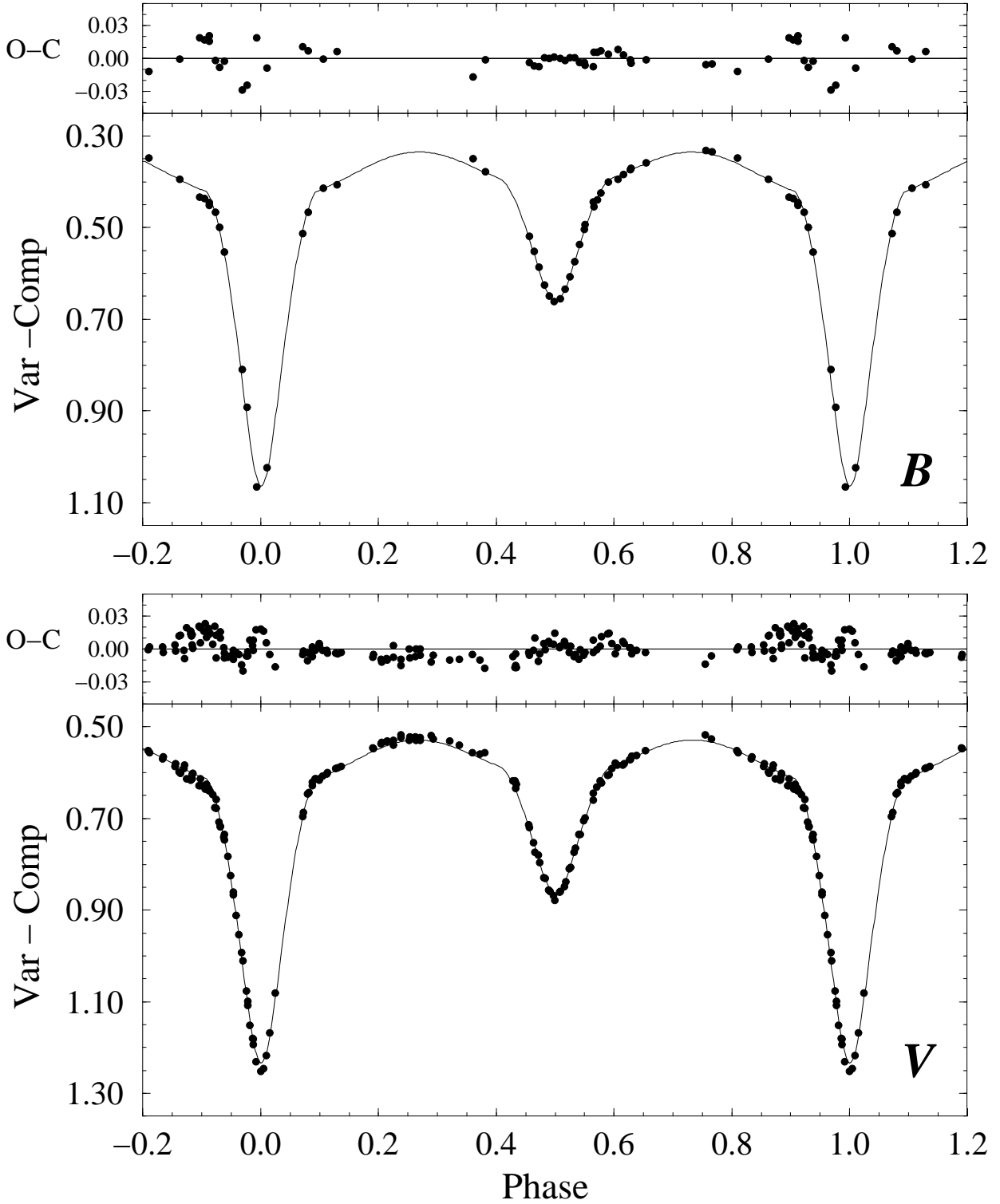


Fig. 4.— *B* and *V* light curves for HV 5936 (filled circles) overplotted with the best fitting model (solid curves). The residuals to the fits (“O-C”) are shown above each light curve. The parameters derived from the fit are listed in Table 2.

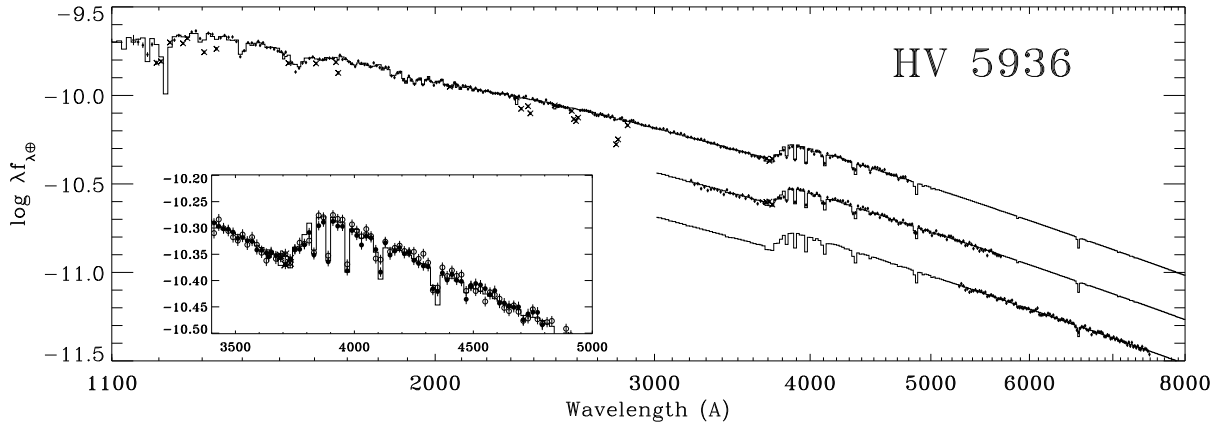


Fig. 5.— The observed UV/optical energy distribution of the HV 5936 system (small filled circles), superimposed with the best-fitting model, consisting of a pair of reddened and distance-attenuated Kurucz ATLAS9 atmosphere models (histogram-style lines). Vertical lines through the data points indicate the 1σ observational errors. Crosses denote data points excluded from the fit, primarily due to contamination by interstellar absorption lines. The top spectrum shows the FOS data, the middle spectrum (shifted by -0.25 dex) the STIS/G430L data, and the lower spectrum (shifted by -0.5 dex) the STIS/G750L data. The energy distribution fitting procedure was performed simultaneously on all three datasets. The inset shows a blowup of the region surrounding the Balmer Jump which illustrates the overlap between the FOS (solid circles) and STIS/G430L (open circles) data. The parameters derived from the fit to the energy distribution are listed in Tables 3, 4, and 5. The various constraints imposed on the fit are discussed in §3.3.3.

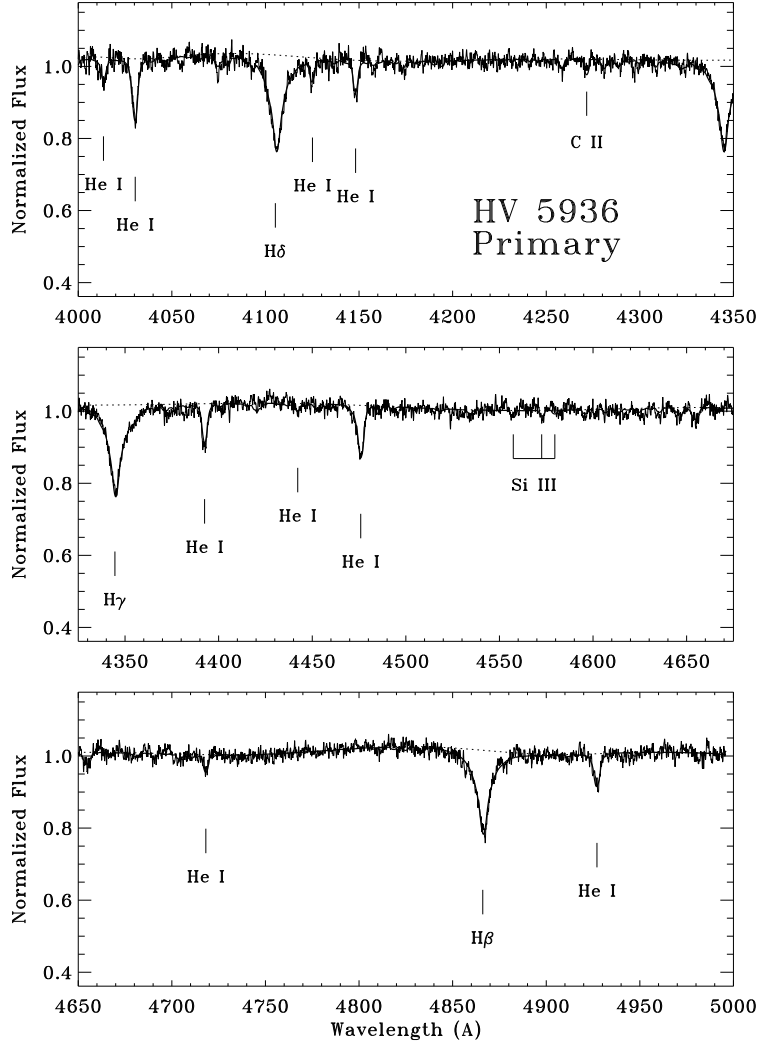


Fig. 6.— “Disentangled” optical spectrum of the primary star in the HV 5936 system, as produced by the KOREL program (see §2). The spectrum consists of 12453 data points, has a spectral resolution of 0.2 \AA , and has been smoothed by 3 points for the presentation. Line strengths in disentangled KOREL spectra are diluted by the presence of continuum light from the companion star. In this case, the companion (i.e., the system’s secondary) contributes about 36.1% of the continuum light and the y-axis of the plots have been adjusted so that the flux zeropoint for the primary’s lines corresponds to the bottom of each panel. The thick solid curve shows a synthetic spectrum fit to the primary’s spectrum, utilizing the ATLAS9 and SYNSPEC programs. This fit included the determination of a 20-order Legendre polynomial to accommodate undulations in the stellar continuum not removed in the original data normalization. See Figure 2 for an example of the original data. The polynomial itself is shown as the dotted line. The stellar properties determined from the fit to the spectrum are consistent with those derived in §3 from the binary and spectral energy distribution analyses. See the discussion in §5 for more information.

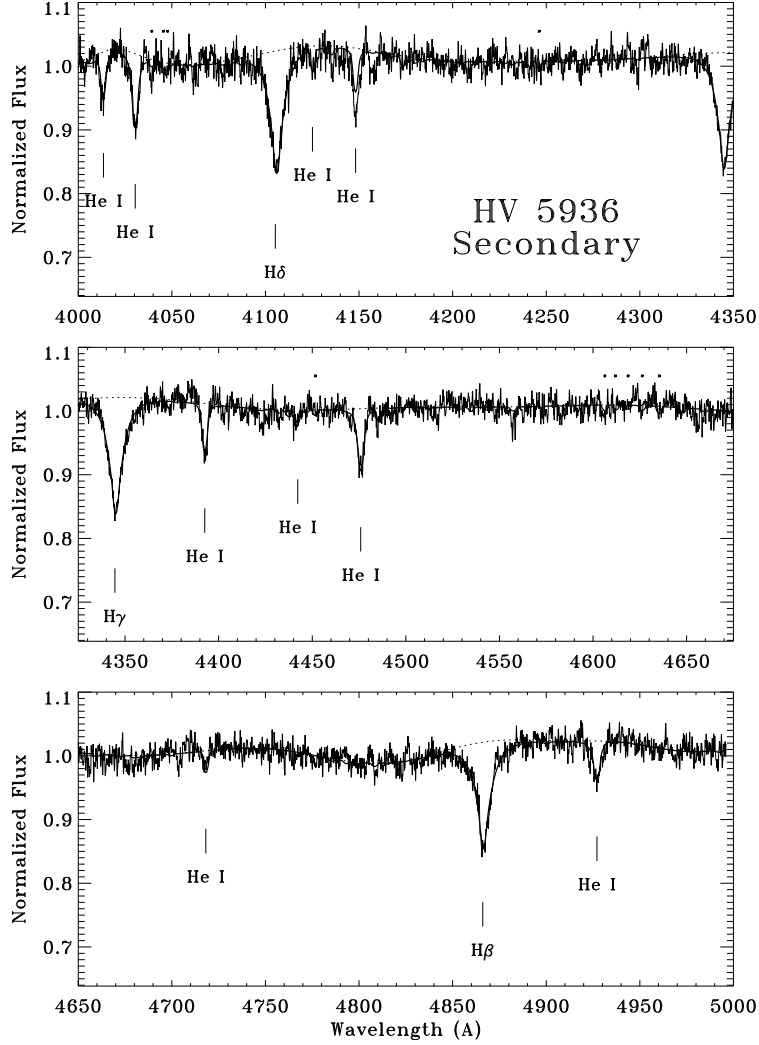


Fig. 7.— Same as Fig. 6 but for the secondary star in the HV 5936 system. In this case, the secondary’s line strengths are diluted by the presence of the primary, which contributes about 63.9% of the continuum light. The flux zeropoint for the secondary corresponds to the bottom of each panel. The synthetic spectrum fit (thick solid curve) included the determination of a 25-order Legendre polynomial (dotted line) to accommodate deficiencies in the original normalization. This fit shown in the figure corresponds to Case II in Table 6 and includes an enhanced He abundance and modified CNO abundances. It reproduces the stellar properties derived independently in §3. The small asterisks indicate the locations of the strongest features of N II. See the discussion in §5 for more information.

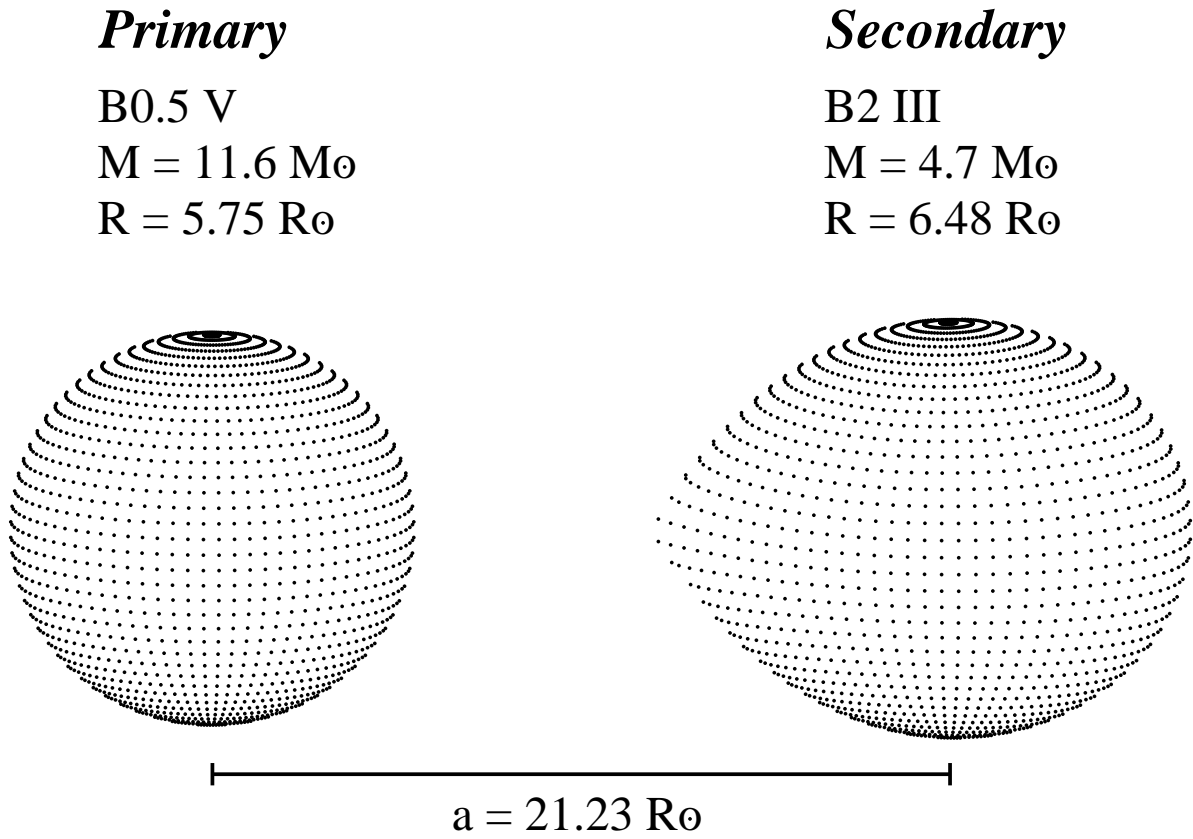


Fig. 8.— A scale model of the HV 5936 system. The sizes of the stars and their separations are shown in their correct proportions.

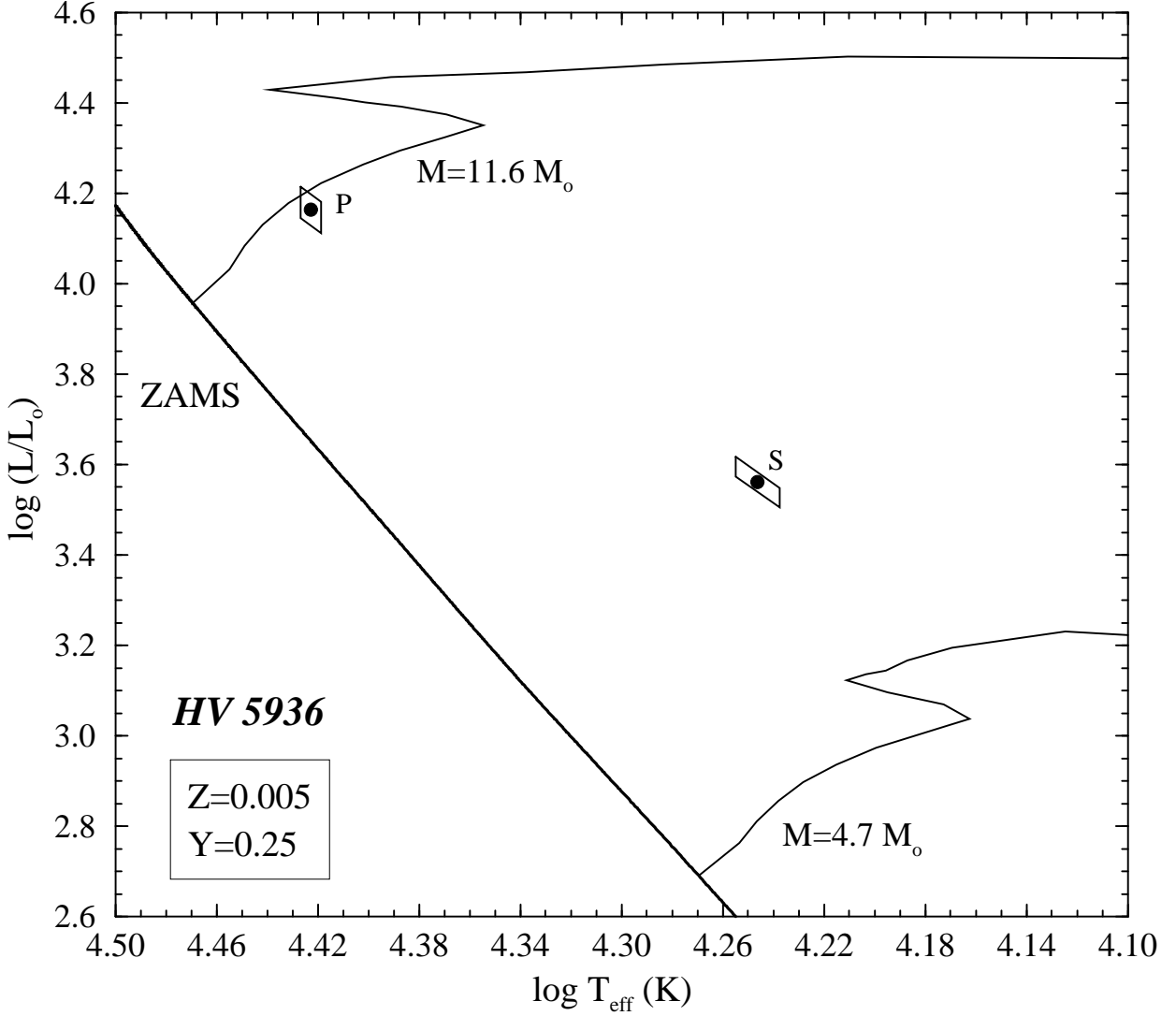


Fig. 9.— A comparison of the HV 5936 results with stellar evolution theory. The positions of the the primary (P) and secondary (S) components on the $\log L$ vs. $\log T_{\text{eff}}$ diagram are indicated by the filled circles. The skewed rectangles represent the 1σ error boxes. The two stellar evolution tracks shown (solid curves) correspond to the masses derived from the binary analysis and the metallicity measured from the UV/optical spectrophotometry. The primary component appears to be in good agreement with stellar evolution model predictions, while the secondary is overluminous for its mass. This same pattern is observed in most of the galactic Algol binaries.

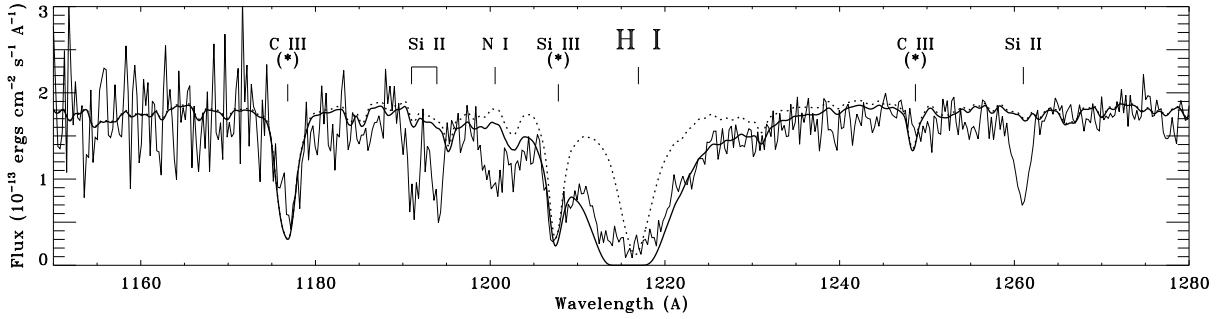


Fig. 10.— Derivation of the interstellar H I column density towards HV 5936. The FOS data centered on the H I Ly α line at 1215.7 Å are shown (thin solid line). Prominent stellar features (denoted with an asterisk) and interstellar features are labeled. The dotted line represents a synthetic spectrum of the HV 5936 system, constructed by combining two individual velocity-shifted spectra. The individual spectra were computed using Ivan Hubeny’s SYNPEC spectral synthesis program with Kurucz ATLAS9 atmosphere models of the appropriate stellar parameters as inputs. The solid curve shows the synthetic spectrum convolved with an interstellar H I Ly α line computed with a Galactic foreground component of $N(\text{H I}) = 5.0 \times 10^{20} \text{ cm}^{-2}$ at 0 km s^{-1} (see text in §4).

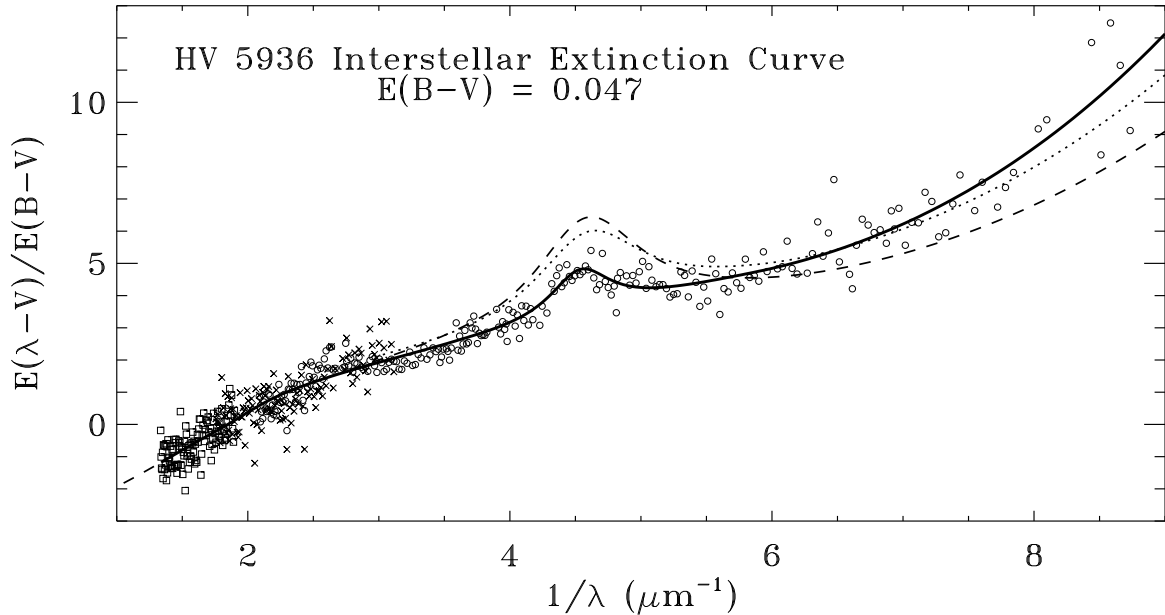


Fig. 11.— Normalized UV-through-optical interstellar extinction curve for HV 5936. The thick solid line shows the parameterized form of the extinction curve as determined by the SED fitting procedure. The recipe for constructing such a “custom” extinction curve is taken from F99 and the parameters defining it are listed in Table 5. Small symbols indicate the actual normalized ratio of model fluxes to observed fluxes: circles, crosses, and squares indicate FOS, STIS G430L, and STIS G750L data, respectively. Shown for comparison are the mean Milky Way extinction curve for $R = 3.1$ from F99 (dashed line) and the mean LMC and 30 Doradus curves from Fitzpatrick (1986; dotted and dash-dotted lines, respectively). Based on the small value of $E(B - V)$, the HV 5936 curve likely arises only from dust in the Milky Way halo.